A general route to nanostructured M[V3O8] and M-x[V6O16] (x=1 and 2) and their first evaluation for building enzymatic biosensors

Nathalie Steunou, Christine Mousty, Olivier Durupthy, Cécile Roux, Guillaume Laurent, Corine Simonnet-Jégat, Jacky Vigneron, Arnaud Etcheberry, Christian Bonhomme, Jacques Livage, et al.

A general route to nanostructured $M[V_3O_8]$ and $M_x[V_6O_{16}]$ ($x = 1$ and 2) and their first evaluation for building enzymatic biosensors†

Nathalie Steunou,*[ab] Christine Mousty,[c] Olivier Durupthy,[a] Cécile Roux,[a] Guillaume Laurent,[a] Corine Simonnet-Jégat,[b] Jacky Vigneron,[b] Arnaud Etcheberry,[b] Christian Bonhomme,[a] Jacques Livage[a] and Thibaud Coradin[a]

Received 25th January 2012, Accepted 16th May 2012
DOI: 10.1039/c2jm30485f

In order to develop novel electroactive hosts for biosensor design, the possibility to use nanostructured vanadate phases as alternatives to well-known V_2O_5 gels was studied. For this purpose, the formation of $M[V_3O_8]$ and $M_x[V_6O_{16}]$ ($x = 1$ and 2) oxides by the sol–gel process has been studied over a wide range of cations ($M^+ = Li^+$, Na^+, K^+, Cs^+, and NH_4^+; $M^{2+} = Ca^{2+}$, Mg^{2+} and Ba^{2+}). By a combination of XRD, ^{51}V NMR and SEM studies, it was possible to evidence the influence of the nature and hydration state of cations on the size and morphology of the resulting particles as well as on the kinetics of their formation. On this basis, $K_2[V_6O_{16}]$ was evaluated for glucose oxidase encapsulation, either *via* impregnation or co-precipitation methods. When compared to V_2O_5, these novel bioelectrodes exhibit higher stability under pH conditions of optimum enzymatic activity, as well as better sensitivity, and reproducibility for glucose detection *via* amperometric titration.

1. Introduction

There is a growing interest towards functional bionanocomposites that act as the active part of an electrochemical, optical or photoelectrical device.[1–4] In particular, cells and enzymes with specific catalytic properties have been combined to inorganic and bioorganic matrices for the building-up of biosensors, bioreactors or biofuel cells.[5] Since the performance of a bioelectrochemical device primarily depends on the stability (under use and storage) of the immobilized biomacromolecules within the matrix and the detection of a measurable signal, current developments focus on new immobilization materials.[6] Until recently, bioencapsulation in inorganic hosts has mainly been performed in silica,[6–8] layered double hydroxides and clay minerals[9] due to their natural origin and/or well-established biocompatibility. In most cases, the function of these inorganic matrices is to preserve the tertiary structure of the biomacromolecules and to avoid their denaturation.[7] However, it has been recently shown that interfacing biomacromolecules with inorganic solids can be successfully extended to non-biogenic phases such as metallic particles and metal oxides.[10–13] Actually, these phases exhibit interesting physical properties that may improve electrochemical systems or allow the design of new bionanotechnological devices.[1,2,14,15] In particular, inorganic phases that exhibit semi-conducting properties have been used to build-up DNA-biochips[16] or neuron-chips.[17] In the same way, one of the critical challenges in the building-up of biosensors and biofuel cells is to promote a direct electron transfer between enzyme and electrodes, which is difficult to achieve because of the location of the prosthetic group within the surrounding protein matrix and consequently the kinetic barrier for electron transfer resulting from the distance between the redox active site and the electrode surface. Since most of the host matrices used so far are non-conductive, the co-insertion of redox mediators or metallic particles within the immobilization matrix is often required.[6,9a] These species can either catalyze a redox reaction with a substrate or shuttle the electrons more efficiently between enzyme and electrode. An alternative promising approach would consist in the encapsulation of enzymes in an electroactive matrix, providing the means for building mediator-free biosensors or third generation biosensors.[9a,18] For most studied bioelectrodes, the electroactive inorganic phase may act as an electron relay to the electrode and thus enhances the electrical

[a]*Chimie de la Matière Condensée de Paris, UMR CNRS 7574, UPMC Paris 6, Collège de France, 11 place Marcelin Berthelot, 75231 Paris Cedex 05, France*
[b]*Institut Lavoisier, UMR CNRS 8180, UVSQ, 45 avenue des Etats-Unis, 78035 Versailles Cedex, France. E-mail: nathalie.steunou@uvsq.fr; Fax: +33 1 39 25 43 73; Tel: +33 1 39 25 44 52*
[c]*Institut de Chimie de Clermont-Ferrand ICCF, CNRS UMR 6296, Université Blaise Pascal, 63177 Aubière Cedex, France*

† Electronic supplementary information (ESI) available: XRD patterns (Fig. S1) of $(NH_4)_2[V_6O_{16}]\cdot H_2O$, $(NH_4)_2[V_6O_{16}]\cdot 1.5H_2O$, $Ca[V_6O_{16}]\cdot 9.7H_2O$, $Mg[V_6O_{16}]\cdot 7.1H_2O$, and $Ba_{1.2}[V_6O_{16}]\cdot 5.5H_2O$; SEM images of $M[V_6O_{16}]\cdot nH_2O$ (with $M^{2+} = Mg^{2+}$, Ca^{2+}, and Ba^{2+}) (Fig. S2) and $K_2[V_6O_{16}]$–GOx biomembrane (Fig. S3); amount of tri- and hexavanadate phases *versus* pH (Fig. S4); the XRD pattern of $V_2O_5\cdot nH_2O$ at pH values of 1, 4 and 5 (Fig. S5); FT-IR spectra of GOx and $K_2[V_6O_{16}]$ (Fig. S6); XPS spectra of $K_2[V_6O_{16}]$ – pH 3, $K_2[V_6O_{16}]$ – pH 6, $K_2[V_6O_{16}]$–GOx (Fig. S7 and S8), and V2p peak positions (Table S1); storage stability of $K_2[V_6O_{16}]$–GOx_{cos} (Fig. S9). See DOI: 10.1039/c2jm30485f

signal of the transducer leading to an improved sensitivity and a lower detection limit of analytes. Currently, the most studied methodology relies on the preparation of composite materials where a conductive network of particles over the percolation threshold (for instance carbon nanotubes) is trapped within a non-conductive matrix, mainly a bio-organic polymer[19] or a sol–gel matrix.[20] Alternatively, it should be possible to use single-phase, conductive oxides obtained *via* the sol–gel process as hosts for enzymes. However, the adaptation of encapsulation procedures developed for silica over the last few years is not straightforward, due to different reactivities (pH, solvent, redox,…) both at the stage of preparation and also in terms of working conditions. This probably explains why non-silica sol–gel based matrices were scarcely employed to entrap enzymes.[18a,b,e,21] Among the potential host candidates, V_2O_5 gels appear to be very interesting due to their conductive, catalytic and intercalation properties that have been widely studied over the last 30 years.[22] However, V_2O_5 is easily reduced by many organic molecules and stable only under acidic conditions, explaining why only two previous reports were devoted to V_2O_5–glucose oxidase (GOx) biosensors.[23,24] In the field of electrochemical devices, the initial interest in V_2O_5 materials has rapidly shifted to other V(v) phases, such as $M[V_3O_8]$ and $M_x[V_6O_{16}]$ ($x = 1$ and 2) (see Fig. 1) for the building-up of positive electrodes for Li-batteries.[25] They were mainly prepared in the literature through hydrothermal and solid state routes. However, numerous studies have demonstrated the strong influence of the grain morphology and the texture of the material on the electrochemical performances of $Li_{1+\alpha}[V_3O_8]$.[25] Since the synthesis of materials through low temperature chemical routes allows a better control of their microstructure and texture, we developed recently a simple sol–gel method for synthesizing nanostructured $M[V_3O_8]$ with monovalent cations $M^+ = Na^+$ [26] and Cs^+.[27]

In the present work, we hypothesized that these phases may also be advantageously developed as an alternative to V_2O_5 for enzyme encapsulation and biosensor design. In a first step, we have tried to extend our previous method to a wide range of cations including divalent ones, to identify the most suitable host for further enzyme encapsulation. An attempt was made to rationalize the effect of the cation size and hydration on the kinetics of formation and structure of the resulting materials. This control over the nucleation and growth of vanadium oxides appears to be crucial for designing new bioelectrochemical devices such as enzymatic biosensors since the control of porosity (organization, pore size, and connectivity) and texture in sol–gel coatings can modulate the enzyme immobilization, and enhance the diffusion of electroactive species, analytes and reaction products. In the second step, we have used (and for the first time to our knowledge) a nanostructured $K_2[V_6O_{16}]\cdot nH_2O$ material to encapsulate glucose oxidase (GOx) as a model enzyme and the resulting bionanocomposites were applied to the electrochemical detection of glucose. These GOx–$K_2[V_6O_{16}]$ biosensors showed superior stability and analytical performance compared to V_2O_5-based systems. The GOx–$K_2[V_6O_{16}]$ biosensors present interesting and very promising properties in terms of sensitivity, reproducibility and response time, showing that vanadium oxides may presumably compete with other inorganic matrices to entrap enzymes. These results raise hope for the future development of third-generation biosensors that would benefit from the chemical, structural and functional versatility of V(v)-based materials.

2. Experimental section

2.1 Synthesis of $M[V_3O_8]$ and $M_x[V_6O_{16}]$ ($x = 1$ and 2)

$M[V_3O_8]$ and $M_x[V_6O_{16}]$ ($x = 1$ and 2) phases (with $M^+ = Na^+$, K^+, Cs^+ and NH_4^+; $M^{2+} = Ca^{2+}$, Mg^{2+} and Ba^{2+}) have been prepared *via* the acidification of an aqueous solution of sodium metavanadate $NaVO_3$ (Sigma, >99%, 0.5 mol L^{-1}, pH = 8) according to the procedure used for the synthesis of vanadium oxide gels.[28] Acidification of a 0.5 mol L^{-1} metavanadate solution ($NaVO_3$), with an initial pH close to 8, was performed using a proton exchange resin (DOWEX 50WX 4–100 mesh). After complete proton exchange, a clear yellow solution (pH $\sim$ 1) is obtained that progressively turns into a red $V_2O_5\cdot nH_2O$ gel after 12 h in the absence of additives. For the synthesis of $M[V_3O_8]$ and $M_2[V_6O_{16}]$ phases, small volumes of MOH and MCl solutions (2 mol L^{-1}) were added to 10 mL of the yellow acidic solution of V(v) precursors in order to set the cation concentration to 0.2 mol L^{-1} and the initial pH (pH_i) to a precise initial value ranging from 1 to 4. The same procedure is used with $M(OH)_2$ and MCl_2 but the concentration of divalent cations is fixed to 0.1 mol L^{-1}. These solutions were then left for ageing at 40 °C for a period between one day and three weeks. Precipitation was observed for all investigated conditions. Table 1 presents the chemical composition of $M_xV_2O_5$ intercalates, $M[V_3O_8]$ and $M_x[V_6O_{16}]$ ($x = 1$ and 2) phases depending on the nature of cation and pH_i, and according to chemical and thermogravimetric analyses and powder X-ray diffraction.

2.2 Synthesis of GOx–$K_2[V_6O_{16}]$ biomembranes

Glucose oxidase (GOx) (E.C. 1.1.3.4. type VII from *Aspergillus niger*, 150–218 U mg^{-1}) was purchased from Sigma. The immobilization of GOx has been performed through a two step adsorption and a co-sedimentation method. For both methods, V_2O_5 sols were first prepared by redispersion of $V_2O_5\cdot nH_2O$ gels in distilled water of pH 5 and homogeneous suspensions of $K_2[V_6O_{16}]\cdot nH_2O$ ($n = 1.5$ and 2.7) were obtained by keeping the aqueous precipitate in an ultrasonic bath for 30 min. Coatings on glass or Pt electrode were prepared by solvent casting from the

$V_2O_5 \cdot nH_2O$ sols and $K_2[V_6O_{16}] \cdot nH_2O$ suspensions and after drying the coatings for about 12 h, a small volume of GOx (10 mg mL^{-1}) in phosphate buffer was then deposited on these films and dried. In order to enhance the lifetime of the biomembrane due to a slow release of enzymes into solution, enzyme cross-linking with glutaraldehyde vapor (GA, 15 min) was performed. The alternative co-sedimentation method consists of mixing together the vanadium oxides and GOx solutions and spreading the aqueous mixture on a substrate. This co-sedimentation method avoids a possible leaching of entrapped enzymes from the biomembranes to the solution and the chemical reticulation step can be skipped. For both immobilization methods, the bioelectrodes are then washed in acetate (V_2O_5 and $K_2[V_6O_{16}]$) or phosphate ($K_2[V_6O_{16}]$) buffers in order to remove the free enzymes before being used as biosensors. The preparation of the Pt modified electrodes is summarized in Table 2, the deposited enzyme amount was fixed at 50 μg.

2.3 Characterization

X-ray powder diffraction patterns were recorded on a Philips PW 1830 diffractometer using CuKα radiation ($\lambda = 1.542$ Å). The FT-IR spectra were recorded on a Nicolet 6700 FT-IR using an Attenuated Total Reflection Infrared (ATR-IR) experiment at a resolution of 4 cm^{-1}. Scanning electron microscopy (SEM) studies were performed on a Cambridge stereoscan 120 microscope using gold-coated samples. Thermogravimetric analyses (TGA) were performed on a TA SDT 2960 apparatus. Solids were heated up to 600 °C with a heating rate of 5 °C min^{-1} in an oxygen atmosphere. The amount of V(IV) in the solids was measured by the spectroscopic UV-visible method according to the previous study.[26] X-ray photoelectron spectroscopy (XPS) surface chemical analyses are performed with a Thermo Electron K-Alpha spectrometer with a base pressure of 5×10^{-10} Torr and using the AlKα (1486.5 eV) X-ray monochromatized radiation with a pass energy of 20 eV. Energy levels of XPS were calibrated with Au single crystal. The spectra were processed using the Thermo Advantage data system. ^{51}V MAS NMR spectra were recorded at 79.0 MHz on a Bruker Avance 300 spectrometer using a 4 mm MAS Bruker probe. Solid samples were spun both at 10 and 14 kHz using ZrO_2 rotors. ^{51}V MAS NMR spectra were acquired with a rotor synchronized echo sequence (θ–τ–2θ–τ-acq. with $\theta = \pi/16$, $\tau = 1/\nu_r$, where ν_r is the spinning frequency) and with power levels corresponding to $\pi/2$ lengths for the liquid standard (NH_4VO_3) of approximately 2.5 μs. A spectral width of 1 MHz and 0.5 s of recycle time were used. Short pulse widths were used to collect a maximum of spinning sidebands with undistorted intensity. An accumulation of 14 000 transients was usually performed on each sample. Isotropic chemical shifts were reported to $VOCl_3$ using a solution of 0.1 mol L^{-1} NH_4VO_3 ($\delta = -578$ ppm) as the secondary reference. The effect of ^1H CW decoupling on the resolution of the ^{51}V MAS NMR spectra was checked. However, no difference in the spectral resolution was observed with or without ^1H decoupling even for the hydrated vanadium oxides. As a consequence, ^{51}V MAS NMR spectra were acquired without ^1H decoupling. Numerical simulations of the ^{51}V MAS NMR spectra were performed with the DMFIT program including the QUASAR extension.[29,30] These simulations included the effects of the chemical shift anisotropy, CSA, as well as first and second-order quadrupolar interactions. Both central and satellite transitions were considered. Several NMR parameters describing the interactions have been determined, including the quadrupole coupling constant (C_Q), the quadrupolar asymmetry parameter (η_Q), the isotropic chemical shift (δ_{iso}), the CSA ($\Delta\delta_{CSA}$) and the CSA asymmetry parameter (η_{CSA}). Chemical shift tensor parameters δ_{iso}, $\Delta\delta_{CSA}$ and η_{CSA} are defined as $\delta_{iso} = (\delta_{11} + \delta_{22} + \delta_{33})/3$, $\Delta\delta_{CSA} = (\delta_{33} - \delta_{iso})$ and

Table 1 Experimental conditions (pH_i and ageing time), chemical composition of (a) $M_xV_2O_5 \cdot nH_2O$ and (b) $M[V_3O_8]$, $M_x[V_6O_{16}]$ ($x = 1$ and 2) phases

Cation	r_{ion}[a] (Å)	pH_i[b]	Chemical composition[c]	d_{001}[d] (Å)	JCPDS/ref.
Li^+	0.74	1–2	$Li_{0.2}V_2O_5 \cdot 2.1H_2O$	12.8	45
Na^+	0.95	1–2	$Na_{0.3}V_2O_5 \cdot 1.5H_2O$	10.4	45 and 46
K^+	1.38	1	$K_{0.4}V_2O_5 \cdot 1.2H_2O$	10.3	45 and 46
Cs^+	1.70	3–4	$4Cs[H_2V_{10}O_{28}] \cdot 4H_2O$	—	80-0431 and 27,36
TMA^+	3.01	1–2	$TMA_{0.27}V_2O_5 \cdot 1.3H_2O$	12.3	45
		3	$4TMA[H_2V_{10}O_{28}] \cdot H_2O$	—	^{51}V MAS and 39
NH_4^+	1.47	1–2	$(NH_4)_{0.3}V_2O_5 \cdot 1.5H_2O$	11.3	45 and 46
Mg^{2+}	0.72	1	$Mg_{0.15}V_2O_5 \cdot 2.4H_2O$	13.8	45
Ca^{2+}	0.99	1–2	$Ca_{0.15}V_2O_5 \cdot 2.0H_2O$	13.8	45
Ba^{2+}	1.36	1	$Ba_{0.15}[V_2O_5] \cdot 1.5H_2O$	12.3	45
		2–4	$3Ba[V_{10}O_{28}] \cdot 21H_2O$		87-1902

Cation	pH_i	Ageing time (days)	Chemical composition	JCPDS/ref.
Na^+	2	21	$Na[V_3O_8] \cdot 1.5H_2O$	16-0601 and 26
	3–4	4	$Na[V_3O_8] \cdot 1.5H_2O$	16-0601 and 26
K^+	2–4	1	$K_2[V_6O_{16}] \cdot 2.7H_2O$	51-0379
			$K_2[V_6O_{16}] \cdot 1.5H_2O$	54-062
Cs^+	1–2	1	$Cs_2[V_6O_{16}]$	84-2497 and 27
	3	21	$Cs_2[V_6O_{16}] \cdot 0.7H_2O$	51-0378 and 27
	3–4	4	$Cs_2[V_6O_{16}]$	84-2497 and 27
NH_4^+	2–4	4	$(NH_4)_2[V_6O_{16}] \cdot H_2O$	41-0492
	3	1	$(NH_4)_2[V_6O_{16}] \cdot 1.5H_2O$	51-0376
Mg^{2+}	2–3	21	$Mg[V_6O_{16}] \cdot 7.1H_2O$	46-0281
Ca^{2+}	2–4	4	$Ca[V_6O_{16}] \cdot 9.7H_2O$	35-0564
Ba^{2+}	2	14	$Ba_{1,2}[V_6O_{16}] \cdot 5.5H_2O$	51-0375

[a] Ionic radius. [b] Initial pH. [c] Phase obtained after 24 h. [d] Basal distance.

Table 2 Amperometric responses to glucose of different metal oxide based biomembranes

Matrix	Imm.[a] (pH)	$Q = G/V$[b]	Sensitivity[c] ($mAM^{-1}\ cm^{-2}$)	R^2 (n)
$K_2[V_6O_{16}]\cdot nH_2O$ (n = 1.5 &2.7)	Ads (5)	0.33	25	0.9994 (12)
	Ads (6)	0.16	48	0.9995 (12)
	Cos (6)	0.16	44	0.9991 (13)
$V_2O_5\cdot nH_2O$	Ads (5)	0.025	17	0.9983 (16)
	Cos (5)	0.025	7.8	0.9990 (18)
V_2O_5 [23]	Cos (6)	—	4.9	
$FeCp_2$[d]–V_2O_5 [24]	Cos (7)	0.8	0.46	
ZrO_2 [47]	Cos (7)		1.42	
TiO_2 [48]	Cos (7)		—	
SiO_2 [48]	Cos (7)		17.6	
ZrO_2/chitosan[49]	Ads (6.5)		0.89	
TiO_2/chitosan[50]	Ads (7.2)		9.25	
ZrO_2/Nafion[47]	Cos (7)		48	
TiO_2/Nafion[48]	Cos (7)		105.7	
SiO_2/Nafion[48]	Cos (7)		71.7	

[a] Imm = immobilization, Ads = adsorption, and Cos = cosedimentation. [b] Q = mass ratio of G = GOx and V = V_2O_5 or $K_2[V_6O_{16}]$. [c] Calculated from the slope of the linear part of the calibration curve. [d] $FeCp_2$ = ferrocene.

$\eta_{CSA} = \frac{(\delta_{22} - \delta_{11})}{(\delta_{33} - \delta_{iso})}$. The quadrupolar parameters are defined as $C_Q = \frac{eQV_{33}}{h}$ and $\eta_Q = \frac{V_{22} - V_{11}}{V_{33}}$. The Euler angles, φ, χ, and ψ, between CSA and quadrupolar tensors were estimated through the careful analysis of both isotropic lines and spinning sidebands. The ^{51}V MAS NMR spectra were fitted with a number of 40 spinning sidebands (SSBs) provided by DMFIT.

2.4 Amperometric titration of glucose

Stock solutions of glucose were allowed to mutarotate at room temperature. Enzymatic activity of immobilized GOx within bionanocomposites casted on glass slides was first verified by measuring the consumption of O_2 in different buffer solutions containing 50 mmol L^{-1} glucose using a Clark electrode. Secondly, the amperometric measurements were carried out with a potentiostat EA161 (EDAQ) connected to a thermostatted cell with a three-electrode system. The working electrodes were platinum electrodes (diameter 5 mm) polished with 1 μm diamond paste and 0.05 μm alumina before use. A Pt wire was used as the counter electrode and all potentials were measured relative to an Ag/AgCl saturated KCl electrode. All measurements were carried out at 30 °C under stirring conditions using a rotating disk electrode from Radiometer (500 rpm). The glucose concentration was increased stepwise by adding in the 20 mL buffer (acetate or phosphate) solution defined volumes of concentrated analyte stock solution. Calibration curves were therefore obtained by measuring the oxidation current of hydrogen peroxide at $E_{app} = 0.7$ V.

3. Results and discussion

3.1 Sol–gel synthesis and characterisation of $M[V_3O_8]$ and $M_x[V_6O_{16}]$ (x = 1 and 2) phases

The synthesis of trivanadate and hexavanadate phases is based on a room temperature process previously reported for the synthesis of sodium and cesium trivanadate (*i.e.* $Na[V_3O_8]$ [26] and $Cs[V_3O_8]$ [27]). In the present work, this procedure was generalized to a large range of monovalent ($M^+ = Li^+$, Na^+, K^+, Cs^+, NH_4^+, and TMA^+(tetramethylammonium)) and divalent cations ($M^{2+} = Ca^{2+}$, Mg^{2+} and Ba^{2+}). All these phases have been fully characterized by combining different techniques (*i.e.* X-ray diffraction, TGA and chemical analysis, UV-vis spectroscopy, ^{51}V MAS NMR spectroscopy and SEM) in order to obtain a precise description of their structure which should be of great benefit when using them in more complex materials such as sensors. The experimental conditions (initial pH and ageing time) and chemical composition of $M[V_3O_8]$ and $M_x[V_6O_{16}]$ (x = 1 and 2) phases are gathered in Table 1(b). The XRD diffraction patterns of solids obtained at $pH_i > 2$ show that they correspond to trivanadate or hexavanadate phases with various amounts of intercalated water (see Table 1(b), Fig. 2 for $M^+ = K^+$ and S1 of ESI†). The molar ratio M/V of these compounds is confirmed by chemical analysis. The amount of water is determined by TGA analysis. The vanadium oxides obtained with Na^+, Mg^{2+}, Ca^{2+} and Ba^{2+} ions are isostructural and this framework can be described as a hewettite type structure (Fig. 1(a)) which is made up of layers with VO_5 trigonal bipyramid chains and distorted VO_6 octahedral chains sharing corners.[31] Vanadium oxide phases with K^+, Cs^+ and NH_4^+ ions exhibit a different vanadium-oxide framework (Fig. 1(b)) made of twisted zigzag chains composed of VO_5 square pyramids sharing corners and edges and distorted VO_6 octahedra.[32] It is worth noting that the geometry of VO_6 and VO_5 polyhedra in these structure types is close. In particular, there is only a slight difference between the angular conformations of a trigonal bipyramid and a square pyramid.[32b] In both structures, cations are intercalated between the layers. The hexavanadate phase of a specific cation (Cs^+, NH_4^+ and Ba^{2+}) may present various amounts of intercalation water depending on initial pH conditions. At the SEM scale, most precipitates consist of rods, which are about 500 nm wide (see Fig. 3(c) and (d) and S2 of ESI†) and a few micrometres long. However, for the same cation, variation of the hydration rate of the vanadium oxide can strongly impact on the particle morphology. As an example, for $(NH_4)_2[V_6O_{16}]\cdot H_2O$, the SEM image shows butterfly like aggregates consisting of elongated platelet crystals which are hundreds μm long and 20 μm wide (Fig. 3(a) and (b)). In

contrast, for $(NH_4)_2[V_6O_{16}]\cdot 1.5H_2O$ the sample is made of entangled fibres of 10 μm long and 200 nm wide (Fig. 3(c)). For $K_2[V_6O_{16}]\cdot nH_2O$, two kinds of crystals are present in the precipitate (see Fig. 3(d), 6 and S3 of ESI†). Spherical aggregates of about 60 μm in diameter are observed that result from the assembly of rods 1–2 μm large together with hexagonal platelets of hundreds μm large (see Fig. 6, *vide infra*). These two kinds of crystals may correspond to the two crystalline structures of $K_2[V_6O_{16}]\cdot nH_2O$ (n = 1.5 and 2.7) that were evidenced by powder XRD (Fig. 2). The local environments of vanadium in the trivanadate and hexavanadate phases were investigated by ^{51}V MAS NMR spectroscopy. The set of ^{51}V parameters extracted from the simulations is listed in Table 3. For both types of structures (*i.e.* hewettite and $K_2[V_6O_{16}]$), the spectra consist of two overlapping manifolds of spinning sidebands representing two resonances that correspond to the two non-equivalent vanadium sites of the asymmetric unit. As an example, Fig. 4(a) and (b) display experimental and simulated ^{51}V MAS NMR spectra of $(NH_4)_2[V_6O_{16}]\cdot H_2O$ that present two resonances at −514 and −551 ppm. The assignment of signals is not straightforward since ^{51}V NMR parameters of both vanadium sites are similar in the hewettite type structure ($M^+ = Na^+$ or $M^{2+} = Ca^{2+}$, Mg^{2+}, and Ba^{2+}) and the $K_2[V_6O_{16}]$ structure type ($M^+ = K^+$, NH_4^+, and Cs^+) (see Table 3). This may be explained by the fact that both vanadium sites exhibit a similar distorted geometry that can be described as a distorted square bipyramid. The coordination sphere of vanadium is composed of a short V=O bond of about 1.6 Å, four V–O bonds of about 1.7–1.9 Å and a long V–O bond (>2 Å) in *trans* position of V=O. A limit of 2.6 Å for V–O distances is generally assumed for including the corresponding oxo ligand in the coordination sphere of vanadium.[33] Depending on this latter bond length, the coordination polyhedron is either close to a square pyramid (for a V–O bond of 2.9 Å) or to a distorted octahedron (for a V–O bond of 2.3 Å). For the $K_2[V_6O_{16}]$ type structure ($M^+ = K^+$, NH_4^+, and Cs^+), one can observe that the $\Delta\delta_{iso}$ parameter is systematically higher for the signal close to −510 ppm (Table 3). As reported previously for a series of polyoxovanadates, this parameter can precisely probe the local distortion of vanadium sites. It was reported that the $|\Delta\delta_{CSA}|$ parameter is typically lower than 320 ppm for VO_4 units in ortho-, pyro- and metavanadates while it is larger than 260 ppm for VO_5 units in divalent metal metavanadates.[34] $\Delta\delta_{CSA}$ parameters are particularly large for strongly distorted VO_6 units in $V_2O_5\cdot nH_2O$ xerogels (≥500 ppm)[26,35] or decavanadate polyanions.[36] Therefore, for $(NH_4)_2[V_6O_{16}]\cdot H_2O$, the signal at −514 ppm with the larger $\Delta\delta_{CSA}$ parameter (−480 ppm) may be assigned to the more distorted vanadium site *i.e.* the site with the square pyramidal environment (V_{sp}). Consequently, the signal at −548 ppm may be attributed to the octahedral site of the structure (V_O). This assignment is in agreement with that reported for $K[V_3O_8]$.[34a] It is quite difficult to distinguish the hewettite and the $K_2[V_6O_{16}]$ type structures on the basis of ^{51}V NMR parameters, since only the values of the isotropic chemical shift (δ_{iso}) are significantly different between the two type structures. Therefore, in this class of compounds, the isotropic chemical shift is certainly influenced by the vanadium oxide framework and the connectivity between vanadium polyhedra. The $K_2[V_6O_{16}]$ type structures ($M^+ = K^+$, NH_4^+, and Cs^+) are characterised by a first signal at $-520 < \delta_{iso} < -510$ ppm and a second at $-551 < \delta_{iso} < -536$ ppm whose difference of δ_{iso} is close to 30–40 ppm (except for $Cs_2[V_6O_{16}]\cdot 0.7H_2O$). In contrast for the hewettite type structure ($M^+ = Na^+$ or $M^{2+} = Ca^{2+}$, Mg^{2+}, and Ba^{2+}), both signals are systematically lower than −520 ppm (*i.e.* one signal at $-547 < \delta_{iso} < -535$ ppm and a second one at $-566 < \delta_{iso} < -548$ ppm) and their difference is reduced to approximately10–20 ppm. The resolution of the ^{51}V spectra seems to depend strongly on the crystallinity and the hydration rate of vanadium oxides. For the hydrated phases (*i.e.* $K_2[V_6O_{16}]\cdot nH_2O$ (n = 1.5 and 2.7), $Mg[V_6O_{16}]\cdot 7.1H_2O$, $Ca[V_6O_{16}]\cdot 9.7H_2O$ and $Ba_{1,2}[V_6O_{16}]\cdot 5.5H_2O$), two very broad signals are present that merge into one single broad resonance in the isotropic part of the spectrum (see Fig. 5). In contrast for $Cs[V_3O_8]$ and $(NH_4)_2[V_6O_{16}]\cdot H_2O$, the isotropic part of the spectrum is composed of two resolved sharp signals. The broadening of the lines possibly results from a distribution of VO_x sites with different local environment (coordinated water molecules, hydrogen bonds,…) as previously evidenced for $Cs_2[V_6O_{16}]\cdot 0.7H_2O$.[27]

To conclude, we have shown that ^{51}V NMR parameters of the hewettite and $K_2[V_6O_{16}]$ structure types are quite close, making difficult the identification of both structures from the NMR point of view. In particular, the similarity of quadrupolar and

Table 3 Isotropic chemical shift (δ_{iso})[a], quadrupole coupling constant (C_Q), quadrupolar asymmetry parameter (η_Q), chemical shift anisotropy ($\Delta\delta_{CSA}$)[a] and CSA asymmetry parameter (η_{CSA})[a] obtained by QUASAR simulations[b] of ^{51}V MAS NMR spectra

Vanadium oxide	δ_{iso} (ppm)	C_Q (kHz)	η_Q	$\Delta\delta_{CSA}$ (ppm)	η_{CSA}	Ref.[c]
$K_2[V_6O_{16}]\cdot 2.7H_2O$[d]	−548	2450	0.44	−405	0	tw
	−510	3030	0.89	−459	0	
$Cs[V_3O_8]$	−548	3000	0.6	−405	0.1	27
	−517	3000	0.7	−460	0.2	
$Cs[V_6O_{16}]\cdot 0.7H_2O$	−536	2200	0.7	−400	0.2	27
	−520	3000	0.8	−460	0.1	
$(NH_4)_2[V_6O_{16}]\cdot nH_2O$	−551	2700	0.3	−420	0.1	tw
$n = 1$ and 1.5[e]	−514	3000	0.8	−480	0.1	
$Na[V_3O_8]\cdot 1.5H_2O$	−548	3100	0.9	−420	0	26
	−535	2400	0.8	−370	0	
$Mg[V_6O_{16}]\cdot 7.1H_2O$	−549	3100	0.9	−420	0	tw
	−538	2400	0.8	−420	0	
$Ca[V_6O_{16}]\cdot 9.7H_2O$	−553	2800	0.7	−370	0.1	tw
	−535	3100	0.4	−400	0.1	
$Ba[V_6O_{16}]\cdot 5.5H_2O$	−566	3000	0.9	−420	0.1	tw
	−547	3000	0.9	−320	0.2	

[a] Chemical shift tensor parameters δ_{iso}, $\Delta\delta_{CSA}$ and η_{CSA} are defined as $\delta_{iso} = (\delta_{11} + \delta_{22} + \delta_{33})/3$, $\Delta\delta_{CSA} = (\delta_{33} - \delta_{iso})$ and $\eta_{CSA} = (\delta_{22} - \delta_{11})/(\delta_{33} - \delta_{iso})$. [b] The data were obtained with the following accuracy : $C_Q \pm 0.1$ MHz; η_Q and $\eta_{CSA} \pm 0.1$; $\delta_{iso} \pm 1$ ppm; $\Delta\delta_{CSA} \pm 10$ ppm; (φ, χ, ψ) close to (0, 60, 0) values. [c] References; tw = this work. [d] For this spectrum, only $K_2[V_6O_{16}]\cdot 2.7H_2O$ was characterized. [e] For $n = 1$ or 1.5, the spectra are almost identical.

CSA parameters between both structure types is consistent with the presence of vanadium sites of similar local environment (strongly distorted VO_5 geometry). Only the isotropic chemical shift parameter with notably different values for both structure types seems to be more sensitive to the vanadium oxide framework.

3.2 Kinetics of transformation of MV_2O_5 intercalates into $M[V_3O_8]$ (or $M_2[V_6O_{16}]$) phases depending on the nature of intercalated cation $M^+(M^{2+})$

In order to select the best candidate for enzyme immobilization, the different tri- and hexavanadates were compared in terms of their kinetics of formation and pH stability range. The synthesis of trivanadates and hexavanadates is based on the preparation of $V_2O_5\cdot nH_2O$ gels at pH $\approx$ 1.5. By adding at constant pH small amounts of cations to an acidic vanadate solution of pH 1, $M_xV_2O_5$ intercalates are first obtained (Table 1(a)). The cation content ($x \sim 0.3$ for M^+ and $x \sim 0.15$ for M^{2+}) (Table 1(a)) obtained by elemental analysis was typically observed for the already prepared $V_2O_5\cdot 1.8H_2O$ xerogel films in which monovalent cations were intercalated.[37,38] By increasing pH above 1 with MOH or $M(OH)_2$ solutions, precipitation of $M[V_3O_8]$ and $M_x[V_6O_{16}]$ ($x = 1$ and 2) phases occurs. Depending on the nature of cation, these vanadium oxides precipitate directly from the vanadate solution or result from the progressive transformation of $M^{I}_{0.3}V_2O_5$ (or $M^{II}_{0.15}V_2O_5$) intercalates.[26] In the first case, the tri- and hexavanadate phases are formed in a short time (1 day) and at very acidic pH (pH 1–2). In the second case, precipitation occurs at higher pH (3–4) and after at least 4 days (Table 1).

The kinetics of formation and thermodynamic stability of the tri- and hexavanadates seem to increase with the ionic radius of interlayer cations (see Table 1 and Fig. S4 of ESI†). Indeed, with the same experimental conditions ($pH_i = 2$, 40 °C), the vanadate phase is fully formed within 21 days with Na^+ while only 1 or 4 days are respectively required with K^+ or NH_4^+ (see Table 1(b)). In fact, three behaviours can be distinguished. For small cations like Mg^{2+}, Na^+, and Ca^{2+} ($r_{ion} < 1$ Å), the formation of trivanadates or hexavanadates takes at least 4 days at pH 3–4. For larger cations like K^+ and NH_4^+ ($1 < r_{ion} < 1.5$ Å), $M[V_3O_8]$ or $M_x[V_6O_{16}]$ ($x = 1$ and 2) can be obtained immediately after one day in the pH range 2–4. Finally for large cations such as Cs^+, TMA^+, and Ba^{2+} ($r_{ion} > 1.35$ Å), a competition is clearly observed between the formation of $M[V_3O_8]$ (or $M_x[V_6O_{16}]$) and that of the decavanadate polyanion. Indeed, it is known that crystallization of polyoxometallates usually requires large cations to occur.[39,40] The kinetics of tri- and hexavanadates formation is particularly low in the pH range 3–4 where the decavanadate is the most abundant vanadate in solution. As an example, cesium tri- or hexavanadate is either obtained after one day at pH 1 or 21 days at pH 3. Therefore, as soon as decavanadate crystalline phases are formed, their dissociation and conversion into tri- or hexavanadate phases are not kinetically or thermodynamically favoured. In the case of the largest TMA^+ cation, it is worth noting that no tri- or hexavanadate phase could be obtained in the pH range 1–4, while precipitation of $4TMA[H_2V_{10}O_{28}]\cdot 4H_2O$ occurs.[39]

The influence of the cation size on the formation of tri- and hexavanadate phases is possibly related to its hydration rate.

Actually, it has been shown previously that the water content of $M_xV_2O_5$ intercalates strongly depends on the size and charge of intercalated cations.[41] For monovalent cations, d_{001} of *ca.* 10.9–11.6 Å typically corresponds to intercalates with one water layer while for divalent cations, the interlamellar space contains two water layers (d_{001} *ca.* 13.4–14.2 Å).[41] An empirical relationship was established showing that the hydration of cations (*i.e.* hydration number) is proportional to the ionic charge to radius ratio *Z*/*r* parameter.[41] Similarly, crystallization of hexavanadate phases of Cs^+ and NH_4^+ ions is obtained respectively with no or only one water molecule per formula unit. In contrast, at least three water molecules *per* $V_6O_{16}^{2-}$ unit are required in the hexavanadate structure for smaller cations like Ba^{2+}, K^+, Mg^{2+} or Ca^{2+}. However the hydration rate of cation does not seem to influence strongly the kinetics of the $M[V_3O_8]$ (or $M_2[V_6O_{16}]$ and $M'[V_6O_{16}]$) formation. As an example, $Ca[V_6O_{16}]\cdot 9.7H_2O$ and $Na[V_3O_8]\cdot 1.5H_2O$ phases are both obtained after 4 days at pH 3 and 4 while the interlayer cations Ca^{2+} and Na^+ have different hydration numbers (*i.e.* 11.0 and 3.4 respectively).[41] In contrast, the kinetics of the $M[V_3O_8]$ (or $M_2[V_6O_{16}]$ and $M'[V_6O_{16}]$) formation seems to be related to the crystallographic structure of the tri- and hexavanadate phases. Indeed, the formation of tri- and hexavanadate phases with the hewettite structural type (Li^+, Na^+, Ca^{2+}, and Mg^{2+}) is systematically delayed compared to those with the $K_2[V_6O_{16}]$ type structure (K^+, Cs^+, and NH_4^+). Since neither the $M_xV_2O_5$ nor the decavanadate polyanion presents a structural relationship with the $M[V_3O_8]$ (or $M_2[V_6O_{16}]$) structures, the formation of these vanadium oxides presumably implies a redissolution–precipitation process whose kinetics are dependent on the size of the cation. It has been previously reported that V_2O_5 gels result from the polycondensation of a neutral precursor $[VO(OH)_3(OH_2)_2]^0$.[22a] Since the composition of the V(v) solution changes with increasing pH, a vanadate solution of pH > 1 presumably contains a mixture of a neutral species $[VO(OH)_3(OH_2)_2]^0$ and a negatively charged precursor $[VO(OH)_4(OH_2)]^-$ as previously reported for the formation of $Na[V_3O_8]\cdot 1.5H_2O$ phases.[26] Both vanadate precursors may be involved in the formation of trivanadate and hexavanadate phases.

3.3 $K_2[V_6O_{16}]\cdot nH_2O$–GOx biosensors: design, stability and performances

Among the different trivanadates and hexavanadates reported in this work, $K_2[V_6O_{16}]\cdot nH_2O$ was selected as an immobilization matrix for enzymes since this phase is obtained in a short time (1 day), with a good yield (see Fig. S4†) and in conditions of moderate acidity (pH > 2). Moreover, since this phase can be obtained at pH close to 4, it may reasonably be expected that it is still stable at 5 < pH < 6, being therefore compatible with a number of enzymes whose activity is optimum, or at least well-preserved, in slightly acidic conditions.

In a first step, we have evaluated the stability of $K_2[V_6O_{16}]\cdot nH_2O$ (n = 1.5 and 2.7) precipitates in aqueous solutions of moderate acidity (typically between pH 3 and 6) in comparison to $V_2O_5\cdot nH_2O$ gels. Preformed V_2O_5 films on a glass support (see ESI† for experimental details) and $K_2[V_6O_{16}]$ precipitates were immersed into acetate buffers of pH 3.5, 4 and 5 and phosphate buffer of pH 6 for about 48 hours. For pH between 3.5 and 5, the colour of V_2O_5 films did not change and these films were not dissociated in solution. Their XRD diagrams (see Fig. S5†) are almost identical to that of a V_2O_5 film at pH 1–2, showing a preservation of the bilayer structure of $V_2O_5\cdot nH_2O$ gels. For pH > 5, the V_2O_5 films evolved rapidly to green amorphous compounds that are dissociated in solution upon ageing. In contrast, the $K_2[V_6O_{16}]$ phase did not evolve in terms of colour and quantity upon ageing in acetate or phosphate buffers at 3.5 < pH < 6 for 48 h. The stability of $K_2[V_6O_{16}]$ at pH 5 and 6 was confirmed by recording the XRD pattern (see Fig. 2) and ^{51}V MAS NMR spectra (see Fig. 5), both being identical to those of the $K_2[V_6O_{16}]\cdot nH_2O$ reference phase at pH 3.

In the second step, we have selected glucose oxidase as a model enzyme for immobilization studies, based on the fact that its optimal activity is close to pH 5.5.[5] The immobilization of GOx has been performed through a two step adsorption and co-sedimentation methods (see Table 2 and Experimental section) both in $K_2[V_6O_{16}]$- and $V_2O_5\cdot nH_2O$ gels for comparison purposes. In both cases, homogeneous thin films of bionanocomposites were formed either on glass or Pt electrodes, as shown in Fig. 6(A) for $K_2[V_6O_{16}]$–GOx. XRD and SEM images of GOx-V_2O_5 films are consistent with a disorganized assembly of V_2O_5 ribbons and GOx, as a result of the enzyme addition to the colloidal solutions of V_2O_5 (see Fig. S5 of ESI†) and in agreement with a previous study.[23] The XRD pattern of $K_2[V_6O_{16}]$ based biomembranes (Fig. 2(b) and (c)) shows that the structure of $K_2[V_6O_{16}]$ is preserved after GOx immobilization by adsorption and co-sedimentation methods. A slight shift in the 00*l* series of reflections is consistent with a slight modification of the interlamellar space and indicates that the enzyme is not intercalated between the vanadium oxide layers. The SEM images of $K_2[V_6O_{16}]$–GOx biomembrane (Fig. 6B(a)–(c)) prepared by adsorption show the coexistence of large platelets a few tens μm large and spherical assemblies of rods about 1–2 μm wide. The SEM image of $K_2[V_6O_{16}]$–GOx biomembranes (Fig. 6B(d)) prepared by co-sedimentation shows a disorganized assembly of both kinds of crystallites.

These $K_2[V_6O_{16}]$–GOx_{cos} were studied by IR spectroscopy, a powerful technique for the determination of the secondary structure of proteins. Indeed, the preservation of the secondary structure of GOx after immobilization in $K_2[V_6O_{16}]$ is crucial in biosensor design since conformational changes can strongly affect the enzyme catalytic activity.[42] The position and relative intensity of main IR absorption peaks for $K_2[V_6O_{16}]$–GOx are listed in Table 4 and compared to those of $K_2[V_6O_{16}]$ and GOx native phases according to the representative FT-IR spectra of the samples (Fig. 7 and S6†).[26,42] The spectrum of $K_2[V_6O_{16}]$–GOx_{cos} presents characteristic vibration modes of GOx and $K_2[V_6O_{16}]$. It has been previously reported that information on the secondary structure of GOx (*i.e.* helices, sheets, coils and turn motifs) can be obtained by analysing the vibration modes of the amide group of the peptide bond (amide I and II bands).[42] For $K_2[V_6O_{16}]$–GOx_{cos}, the main peptide absorption bands at 1648 cm^{-1} (ν C=O amide I) and 1547 cm^{-1} (δ N–H amide II) are quite close to those of the native GOx (*i.e.* 1652 cm^{-1} and 1540 cm^{-1} respectively). The position and the relative intensity of these vibration bands in the FT-IR spectrum of $K_2[V_6O_{16}]$–GOx_{cos} are consistent with the assignment of both vibration modes, suggesting that the secondary structure and

consequently the bioactivity of GOx after immobilization in the vanadium oxide are preserved. Moreover, the FT-IR spectrum of $K_2[V_6O_{16}]$–GOx_{cos} shows other characteristic vibrational modes of GOx (*i.e.* amide III and carbon skeleton vibrations in the 1000–1500 cm^{-1} range) (see Table 4). Finally, the FT-IR spectra of $K_2[V_6O_{16}]$–GOx_{cos} and $K_2[V_6O_{16}]$ exhibit typical absorption peaks of V–O stretching modes at close wavenumber positions, suggesting that the vanadium oxide skeleton is preserved after association with GOx.

After the immobilization of GOx in both $K_2[V_6O_{16}]\cdot nH_2O$ (n = 1.5 and 2.7) and $V_2O_5\cdot nH_2O$, the colour of the bio-hybrid membranes turns brown, revealing a slight reduction of V^{5+} to V^{4+} for V_2O_5 and $K_2[V_6O_{16}]\cdot nH_2O$. The surface $[V^{5+}]/[V^{4+}]$ composition has been determined by X-ray photoelectron spectroscopy. Fig. S7 and S8† display the V 2p, K2p and C1s XPS spectra of the $K_2[V_6O_{16}]$ reference phase at pH 3 (*i.e.* $K_2[V_6O_{16}]$ – pH 3), the $K_2[V_6O_{16}]$ phase obtained after immer-sion in a phosphate buffer solution of pH 6 for 24 h (*i.e.* $K_2[V_6O_{16}]$ – pH 6) and $K_2[V_6O_{16}]$–GOx_{cos}. The K2p XPS spectra of the three samples can be fully superimposed revealing a similar K^+ environment in the three compounds. The $V2p_{3/2}$ spectra of the three compounds are quite similar and display a broad peak that can be fitted with two components close to 515.8 and 517.0 eV that can be assigned respectively to V^{4+} and V^{5+} species.[43] The amount of V^{4+} and V^{5+} surface species could be extracted from the peak area ratios (see Table S1†) and a trend of the $[V^{5+}]/[V^{4+}]$ ratio evolution can be given. According to these results, the reduction of V^{5+} by mixing $K_2[V_6O_{16}]$ in a phosphate buffer at pH 6 is not significant. However, the encapsulation of GOx in $K_2[V_6O_{16}]$ leads presumably to a more significant reduction of V^{5+} since the $[V^{5+}]/[V^{4+}]$ composition evolves roughly from 19 to 12. The reduction of vanadium(V) to vanadium(IV) can enhance the electronic conductivity of vanadium oxides due to the electron hopping between V^{5+} and V^{4+}. Therefore, the biosensor response may take advantage of the electronic properties of vanadium oxides that may enhance the rate of electron transfer, thereby increasing the intensity of the electrical signal and decreasing the detection limit of the analytes.

Finally, $K_2[V_6O_{16}]$–GOx films were evaluated as biosensors for glucose detection without mediator using amperometric titration. Glucose oxidase (GOx) catalyzes the aerobic oxidation of glucose with concomitant production of H_2O_2:

Table 4 Main peaks in the FT-IR spectra of $K_2[V_6O_{16}]$–GOx_{cos}, $K_2[V_6O_{16}]$ and GOx samples and corresponding assignments[a]

GOx	$K_2[V_6O_{16}]\cdot nH_2O$	$K_2[V_6O_{16}]$–GOx_{cos}	
Wavenumber cm^{-1} (intensity)	Wavenumber cm^{-1} (intensity)	Wavenumber cm^{-1} (intensity)	Assignments
		3539 (sh)	ν O–H·(H_2O)
	3406 (br)	3402 (br)	ν O–H·(H_2O)
3285 (br)			ν N–H (amide)
3065 (vw)			
2961 (w)		2957 (w)	ν C–H
2929 (w)		2929 (w)	ν C–H
2872 (w)		2878 (w)	ν C–H
	1645 (s)		δ H–O–H·(H_2O)
1652 (s)		1648 (s)	ν C=O (amide I)
1540 (m)		1547 (m)	δ N–H (amide II)
1452 (w)		1458 (w)	
1391 (w)		1397 (w)	
1344 (w)		1347 (w)	
1302 (w)		1302 (w)	
1245 (w)		1251 (w)	(Amide III)
1086 (br)		1096 (br)	
953 (vw)			
	1004 (w)	1000 (m)	ν V=O
	969 (w)	965 (m)	ν V=O
	950 (w)	953 (m)	ν V=O
826 (vw)			
	729 (w)	737 (m)	ν O–V–O
	657 (w)	660 (m)	ν O–V–O
	520 (w)	523 (m)	ν O–V–O

[a] br = broad, m = medium, sh = shoulder, s = strong, w = weak, and vw = very weak.

$$\text{Glucose} + O_2 = \text{gluconolactone} + H_2O_2$$

A significant activity of GOx (by measuring the consumption of O_2) was detected in those biomembranes soaked in 50 mmol L^{-1} glucose solutions at 3.5 < pH < 5 for V_2O_5 and 3.5 < pH < 6 for $K_2[V_6O_{16}]$, demonstrating the possibility of sensing analytes in a large pH range. After 24 h of storage at 4 °C, the bioelectrodes still present a GOx activity. These preliminary experiments show that vanadium oxides can serve as a host matrix for GOx encapsulation and preserve the biocatalytic activity at pH between 3.5 and 6. The amperometric titration of glucose was therefore performed by using $V_2O_5{\cdot}nH_2O$ gels and $K_2[V_6O_{16}]$ matrices in acetate (pH 5) or phosphate buffer (pH 6) solutions. These pH values were chosen since they are close to the optimum pH of native GOx, namely pH 6.0 and in the pH stability range of the studied vanadium oxides. In order to determine the best configuration for the glucose determination, two different amounts (50 and 100 μg) of GOx were immobilized by the adsorption method. Since the biosensor response was not improved using the higher amount, the quantity of GOx was fixed at 50 μg in all biomembranes. The electrochemical responses to successive additions of glucose were recorded with rotating disk Pt electrodes at 0.7 V/Ag/AgCl which is in the potential range of hydrogen peroxide oxidation. Typical calibration curves of V_2O_5 and $K_2[V_6O_{16}]$ based on steady state measurement are depicted in Fig. 8. For both $V_2O_5{\cdot}nH_2O$ gels and $K_2[V_6O_{16}]$ matrices, the bioelectrodes present rapid (t = 15 s), stable and sensitive responses to glucose additions whatever the preparation method (adsorption and co-sedimentation). Both types of bioelectrodes provide an excellent linear relationship to glucose concentration with a dynamic concentration range between 2.5×10^{-5} M and 1.5×10^{-3} M or 3.0×10^{-3} M for $K_2[V_6O_{16}]$ and $V_2O_5{\cdot}nH_2O$ gels, respectively. The sensitivities are calculated from the slope of the linear part of these calibration curves (Table 2). The comparison of the sensitivities of both matrices at pH 5 shows that the performance of $K_2[V_6O_{16}]$ is superior to $V_2O_5{\cdot}nH_2O$. Moreover, immobilisation of GOx by co-sedimentation with V_2O_5 caused a strong decrease of the sensitivity value presumably due to a partial denaturation of enzymes when mixed with this matrix. $K_2[V_6O_{16}]$ appears to be more biocompatible. The same high value of sensitivity (44–48 mM M^{-1} cm^{-2}) is obtained with $K_2[V_6O_{16}]$ at pH 6 whatever the immobilization method, in agreement with a better preservation of GOx bioactivity in phosphate buffer at pH 6 compared to that in acetate buffer at pH 5 for which the sensitivity is twice as low. The same tendency is observed with the maximum current densities at saturating glucose conditions (J_{max}) which reflects the amount of immobilized proteins exhibiting an electro-enzymatic activity. Indeed the value of J_{max} is two times lower at pH 5 (42 μA cm^{-2}) than at pH 6 (88–78 μA cm^{-2}).

In order to estimate the repeatability, the reproducibility and the storage stability of our glucose biosensor, we have selected the $K_2[V_6O_{16}]$–GOx_{cos} biosensor at pH 6. The repeatability of response current was investigated for ten successive additions of 10 μM glucose (Fig. 8(C)). The relative standard deviation coefficient (RSD) was 6%. The detection limit determined for a signal to noise ratio of 3 was 5 μM. Four electrodes, made independently, showed a reproducibility of 6.5%. Two $K_2[V_6O_{16}]$–GOx_{cos} electrodes were stored in phosphate buffer solution (pH 6) at 4 °C to study their storage stability for four weeks. The biosensor responses as a function of storage time correspond to an average value of 5 measurements (10 μM glucose). The biosensor responses were stable for one week, afterwards a slow decrease of the signal was observed. After four weeks, the biosensor responses were around 40% of their initial value (Fig. S9†).

To the best of our knowledge, there are only two other reports dealing with V_2O_5–GOx based biosensors in the literature, involving either thin films of reduced V_2O_5[23] or nanocomposites based on $V_2O_5{\cdot}nH_2O$ gels intercalated by ferrocene ($FeCp_2$) and mixed with a polymer matrix (PVA).[24] Ferrocene serves as a reducing agent of V(v) as well as a redox mediator for the enzyme regeneration. Compared to the pure mediator system ($FeCp_2$/PVA),[24] the biosensor displays 20% increase of sensitivity. In both previous studies, the biosensor performance is promising and is certainly due to the electrical conductivity of V_2O_5. In particular, the vanadium oxide framework can establish the electron communication between the electrode surface and $FeCp_2$ or GOx, thereby enhancing the electrical signal of the transducer and leading to an improved sensitivity and a lower detection limit of analytes. In this context, the performance of the here-described $K_2[V_6O_{16}]$–GOx membranes was compared to those calculated for other biosensors using V_2O_5[23,24] (Table 2). The sensitivities obtained in the present work are significantly higher than those reported in these two systems, showing that $K_2[V_6O_{16}]{\cdot}nH_2O$ (n = 1.5 and 2.7) is a more suitable matrix for enzyme encapsulation than V_2O_5. Similarly, these biosensor performances can also be compared to those reported for other glucose biosensors based on metal oxide/Pt electrodes (Table 2).

The sensitivities of the present biosensors are higher than other GOx biosensors based on sol–gel metal oxides (ZrO_2 and SiO_2) (see Table 2). Since cracks and fractures are often observed in dry monolithic sol–gel metal oxide films, composite electrodes can be alternatively prepared by adding organic polymers (chitosan or Nafion) into sol–gel solutions. The use of Nafion appears to be particularly efficient, with the best sensitivities for TiO_2 and SiO_2. In the present work, the vanadium oxide films are quite homogeneous and stabilization by adding another organic component is not necessary, giving rise to quite good sensitivity, detection limit and storage stability.

4. Conclusion

There is currently a strong demand for functional materials that can be formed and/or can operate under conditions compatible with the preservation of biological activities. In terms of chemistry, these conditions, *i.e.* moderate temperature, near neutral pH, no organic solvents, and toxicity, are binding enough to disqualify a number of well-known materials. Therefore, there is a need to explore more widely the diversity of materials composition and structures to identify suitable candidates for bionanocomposite design.

Looking for potential electroactive hosts for the building-up of enzymatic biosensors, we have shown that the room temperature process leading to the synthesis of $Na[V_3O_8]\cdot 1.5H_2O$ can be extended to a large range of cations including divalent ones. This chemical route leads to nanostructured tri- and hexavanadate phases with either the hewettite- or $K_2[V_6O_{16}]$ type crystalline structures. The size and morphology of crystallites depend both on the nature of cation and hydration rate of the oxides, showing the possibility of finely tuning the texture of the material by this process. We have observed that the kinetics of the formation of vanadium oxides with the $K_2[V_6O_{16}]$ type structure (*i.e.* K^+, Cs^+, and NH_4^+) is significantly enhanced compared to those with the hewettite-type structure (*i.e.* Li^+, Na^+, Ca^{2+}, and Mg^{2+}). Finally, the nanostructured $K_2[V_6O_{16}]\cdot nH_2O$ material has been used for the first time to build up enzymatic based biosensors. The $K_2[V_6O_{16}]$ based amperometric biosensor presents superior properties to $V_2O_5\cdot nH_2O$ gels in terms of sensitivity and reproducibility, showing that these phases may presumably compete with other inorganic host matrices through the optimization of the biosensor preparation. The good stability of $K_2[V_6O_{16}]\cdot nH_2O$ in a large pH range and different buffers shows that this matrix is apparently tunable to a wide range of specific conditions (pH, buffer,…), allowing the extension of this approach to a wide range of enzymes and sensing analytes even at low pH values. Further developments are now necessary to fully take advantage of the electrocatalytic activity of $K_2[V_6O_{16}]\cdot nH_2O$ in sensing devices, including composite approaches involving biopolymers that should increase the bio-compatibility of the host material as well as widen the pH range of stability.[44] Moreover, an increase of the V^{4+} content may enhance the rate of the electron transfer thereby increasing the sensitivity of the bioelectrodes.

References

1 (*a*) M. Darder, P. Aranda and E. Ruiz-Hitzky, *Adv. Mater.*, 2007, **19**, 1309; (*b*) E. Ruiz-Hitzky, M. Darder and P. Aranda, *J. Mater. Chem.*, 2005, **15**, 3650.

2 (*a*) S. Mann, *Nat. Mater.*, 2009, **8**, 781; (*b*) A. J. Patil and S. Mann, *J. Mater. Chem.*, 2008, **18**, 4605.

3 A. Walcarius, D. Mandler, J. A. Cox, M. Collinson and O. Lev, *J. Mater. Chem.*, 2005, **15**, 3663.

4 M. I. Shukoor, F. Natalio, H. A. Therese, M. N. Tahir, V. Ksenofontov, M. Panthöfer, M. Eberhardt, P. Theato, H. C. Schröder, W. E. G. Müller and W. Tremel, *Chem. Mater.*, 2008, **20**, 3567.

5 I. Willner and E. Katz, *Angew. Chem., Int. Ed.*, 2000, **39**, 1180.

6 (*a*) V. B. Kandimalla, V. S. Tripathi and H. Ju, *Crit. Rev. Anal. Chem.*, 2006, **36**, 73; (*b*) Z. Xu, X. Chen and S. Dong, *TrAC, Trends Anal. Chem.*, 2006, **25**(9), 899; (*c*) W. Jin and J. D. Brennan, *Anal. Chim. Acta*, 2002, **461**, 1.

7 (*a*) D. Avnir, T. Coradin, O. Lev and J. Livage, *J. Mater. Chem.*, 2006, **16**, 1013; (*b*) A. C. Pierre, *Biocatal. Biotransform.*, 2004, **22**(3), 145; (*c*) D. Avnir, S. Braun, O. Lev and M. Ottolenghi, *Chem. Mater.*, 1994, **6**, 1605.

8 J. Livage, T. Coradin and C. Roux, *J. Phys.: Condens. Matter*, 2001, **13**, R673.

9 (*a*) C. Mousty, *Appl. Clay Sci.*, 2004, **27**, 159; (*b*) C. Forano, S. Vial and C. Mousty, *Curr. Nanosci.*, 2006, **2**, 283; (*c*) C. Mousty, *Anal. Bioanal. Chem.*, 2010, **396**, 315.

10 F. Natalio, R. André, S. A. Pihan, M. Humanes, R. Wever and W. Tremel, *J. Mater. Chem.*, 2011, **21**, 11923.

11 Z. Schnepp, S. R. Hall, M. J. Hollamby and S. Mann, *Green Chem.*, 2011, **13**, 272.

12 M. N. Tahir, R. André, J. K. Sahoo, F. D. Jochum, P. Theato, F. Natalio, R. Berger, R. Branscheid, U. Kolb and W. Tremel, *Nanoscale*, 2011, **3**, 3907.

13 R. Ben-Knaz and D. Avnir, *Biomaterials*, 2009, **30**, 1263.

14 A. I. Ruiz, M. Darder, P. Aranda, R. Jimenez, H. Van Damme and E. Ruiz-Hitzky, *J. Nanosci. Nanotechnol.*, 2006, **6**, 1602.

15 S.-J. Choi, Y.-C. Lee, M.-L. Seol, J.-H. Ahn, S. Kim, D.-I. Moon, J.-W. Han, S. Mann, J.-W. Yang and Y.-K. Choi, *Adv. Mater.*, 2011, **23**, 3979.

16 (*a*) V. Stambouli, A. Zebda, E. Appert, C. Guiducci, M. Labeau, J.-P. Diard, B. Le Gorrec, N. Brack and P. J. Pigram, *Electrochim. Acta*, 2006, **51**, 5206; (*b*) A. Zebda, V. Stambouli, M. Labeau, C. Guiducci, J.-P. Diard and B. Le Gorrec, *Biosens. Bioelectron.*, 2006, **22**, 178.

17 (*a*) M. Ulbrich and P. Fromherz, *Adv. Mater.*, 2001, **13**, 344; (*b*) M. Merz and P. Fromherz, *Adv. Funct. Mater.*, 2005, **15**, 739.

18 (*a*) Y. Zhang, P. He and N. Hu, *Electrochim. Acta*, 2004, **49**, 1981; (*b*) L. Zhang, Q. Zhang, X. Lu and J. Li, *Biosens. Bioelectron.*, 2007, **23**, 102; (*c*) Z. Dai, S. Liu and H. Ju, *Electrochim. Acta*, 2004, **49**, 2139; (*d*) M. Elkaoutit, I. Naranjo-Rodriguez, M. Dominguez, M. P. Hernandez-Artiga, D. Bellido-Milla and J. L. Hidalgo-Hidalgo de Cisneros, *Electrochim. Acta*, 2008, **53**, 7131; (*e*) P. Si, S. Ding, J. Yuan, X. W. Lou and D.-H. Kim, *ACS Nano*, 2011, **5**(9), 7617; (*f*) W. Zhang and G. Li, *Anal. Sci.*, 2004, **20**, 603; (*g*) F. Tasca, M. N. Zafar, W. Harreither, G. Nöll, R. Ludwig and L. Gorton, *Analyst*, 2011, **136**(10), 2033.

19 M. Zhang, A. Smith and W. Gorski, *Anal. Chem.*, 2004, **76**, 5045.

20 D. Ivnitski, K. Artyushkova, R. A. Rincon, P. Atanassov, H. R. Luckarift and G. R. Johnson, *Small*, 2008, **4**, 357.

21 (*a*) M. Viticoli, A. Curulli, A. Cusma, S. Kaciulis, S. Nunziante, L. Pandolfi, F. Valentini and G. Padeletti, *Mater. Sci. Eng., C*, 2006, **26**, 947; (*b*) Z. Liu, J. Deng and D. Li, *Anal. Chim. Acta*, 2000, **407**, 87.

22 (*a*) J. Livage, *Chem. Mater.*, 1991, **3**, 578; (*b*) Y. Wang and G. Cao, *Chem. Mater.*, 2006, **18**, 2787; (*c*) B. Casal, E. Ruiz-Hitzky, M. Crespin, D. Tinet and J. C. Galvan, *J. Chem. Soc., Faraday Trans. 1*, 1989, **85**, 4167.

23 V. Glezer and O. Lev, *J. Am. Chem. Soc.*, 1993, **115**, 2533.

24 C. G. Tsiafoulis, A. B. Florou, P. N. Trikalitis, T. Bakas and M. I. Prodromidis, *Electrochem. Commun.*, 2005, **7**, 781.

25 (*a*) K. West, B. Zachau-Christiansen, S. Skaarup, Y. Saidi, J. Barker, I. I. Olsen, R. Pynenburg and R. Koksbang, *J. Electrochem. Soc.*, 1996, **143**, 820; (*b*) M. Dubarry, J. Gaubicher, D. Guyomard, N. Steunou and J. Livage, *Chem. Mater.*, 2004, **16**, 4867; (*c*) M. Dubarry, J. Gaubicher, D. Guyomard, O. Durupthy, N. Steunou, J. Livage, N. Dupre and C. Grey, *Chem. Mater.*, 2005, **17**, 2276.

26 O. Durupthy, N. Steunou, T. Coradin, J. Maquet, C. Bonhomme and J. Livage, *J. Mater. Chem.*, 2005, **15**, 1090.
27 O. Durupthy, J. Maquet, C. Bonhomme, T. Coradin, J. Livage and N. Steunou, *J. Mater. Chem.*, 2008, **18**, 3702.
28 J. Lemerle, L. Nejem and J. Lefebvre, *J. Inorg. Nucl. Chem.*, 1980, **42**, 17.
29 D. Massiot, F. Fayon, M. Capron, I. King, S. Le Calvé, B. Alonso, J.-O. Durand, B. Bujoli, Z. Gan and G. Hoatson, *Magn. Reson. Chem.*, 2002, **40**, 70.
30 J. P. Amoureux, C. Fernandez and Y. Dumazy, *37th Rocky Mountain Conference*, Denver, 1995, Abstract no. 264; J. P. Amoureux and C. Fernandez, *QUASAR – Solid State NMR Simulation for Quadrupolar Nuclei*, University of Lille, France, this program is accessible within Dmfit 2004 at http://www.cemhti.cnrs-orleans.fr/dmfit/.
31 (*a*) A. D. Wadsley, *Acta Crystallogr.*, 1957, **10**, 261; (*b*) H. T. Evans, *Can. Mineral.*, 1989, **27**, 181; (*c*) Y. Oka, T. Yao, S. Sato and N. Yamamoto, *J. Solid State Chem.*, 1998, **140**, 219.
32 (*a*) Y. Oka, T. Yao and N. Yamamoto, *Mater. Res. Bull.*, 1997, **32**, 1201; (*b*) H. T. Evans and S. Block, *Inorg. Chem.*, 1966, **5**, 1808; (*c*) A. D. Kelmers, *J. Inorg. Nucl. Chem.*, 1961, **21**, 45; (*d*) B.-Z. Lin and S.-X. Liu, *Acta Crystallogr., Sect. C: Cryst. Struct. Commun.*, 1999, **55**, 1961.
33 P. Y. Zavalij and M. S. Whittingham, *Acta Crystallogr., Sect. B: Struct. Sci.*, 1999, **55**, 627.
34 (*a*) J. Skibsted, N. C. Nielsen, H. Bildsoe and H. J. Jakobsen, *J. Am. Chem. Soc.*, 1993, **115**, 7351; (*b*) J. Skibsted, C. J. H. Jacobsen and H. J. Jakobsen, *Inorg. Chem.*, 1998, **37**, 3083; (*c*) U. G. Nielsen, H. J. Jakobsen and J. Skibsted, *Inorg. Chem.*, 2000, **39**, 2135; (*d*) U. G. Nielsen, H. J. Jakobsen and J. Skibsted, *J. Phys. Chem. B*, 2001, **105**, 420.
35 (*a*) C. J. Fontenot, J. W. Wiench, M. Pruski and G. L. Schrader, *J. Phys. Chem. B*, 2001, **105**, 10496; (*b*) C. J. Fontenot, J. W. Wiench, G. L. Schrader and M. Pruski, *J. Am. Chem. Soc.*, 2002, **124**, 8435.
36 L. A. Truflandier, F. Boucher, C. Payen, R. Hajjar, Y. Millot, C. Bonhomme and N. Steunou, *J. Am. Chem. Soc.*, 2010, **132**, 4653.
37 L. Znaidi, N. Baffier and D. Lemordant, *Solid State Ionics*, 1988, **28–30**, 1750.
38 A. Bouhaouss, P. Aldebert, N. Baffier and J. Livage, *Rev. Chim. Miner.*, 1985, **22**, 417.
39 L. Bouhedja, N. Steunou, J. Maquet and J. Livage, *J. Solid State Chem.*, 2001, **162**, 315.
40 (*a*) B. Pecquenard, P. Y. Zavalij and M. S. Whittingham, *Acta Crystallogr., Sect. C: Cryst. Struct. Commun.*, 1998, **54**, 1833; (*b*) G. Rigotti, B. E. Rivero and E. E. Castellano, *Acta Crystallogr., Sect. C: Cryst. Struct. Commun.*, 1987, **43**, 197; (*c*) P. Roman, A. Aranzabe, A. Luque, J. M. Gutierrez-Zorrilla and M. Martinez-Ripoll, *J. Chem. Soc., Dalton Trans.*, 1995, 2225.
41 N. Baffier, L. Znaidi and J.-C. Badot, *J. Chem. Soc., Faraday Trans.*, 1990, **86**(14), 2623.
42 (*a*) Q. Wang, W. Xu, P. Wu, H. Zhang, C. Cai and B. Zhao, *J. Phys. Chem. B*, 2010, **114**, 12754; (*b*) W.-Z. Jia, K. Wang, Z.-J. Zhu, H.-T. Song and X.-H. Xia, *Langmuir*, 2007, **23**, 11896; (*c*) M. Portaccio, B. Della Ventura, D. G. Mita, N. Manolova, O. Stoilova, I. Rashkov and M. Lepore, *J. Sol-Gel Sci. Technol.*, 2011, **57**, 204.
43 J. Mendialdua, R. Casanova and Y. Barbaux, *J. Electron Spectrosc. Relat. Phenom.*, 1995, **71**, 249.
44 (*a*) F. Carn, O. Durupthy, B. Fayolle, T. Coradin, G. Mosser, M. Schmutz, J. Maquet, J. Livage and N. Steunou, *Chem. Mater.*, 2010, **22**, 398; (*b*) F. Carn, N. Steunou, M. Djabourov, T. Coradin, F. Ribot and J. Livage, *Soft Matter*, 2008, **4**, 735; (*c*) F. Carn, M. Djabourov, T. Coradin, J. Livage and N. Steunou, *J. Phys. Chem. B*, 2008, **112**, 12596.
45 T. Yao, Y. Oka and N. Yamamoto, *Mater. Res. Bull.*, 1992, **27**, 669.
46 T. Yao, Y. Oka and N. Yamamoto, *J. Mater. Chem.*, 1992, **2**, 331.
47 H.-J. Kim, S. H. Yoon, H. N. Choi, Y.-K. Lyu and W.-Y. Lee, *Bull. Korean Chem. Soc.*, 2006, **27**, 65.
48 H. N. Choi, M. A. Kim and W.-Y. Lee, *Anal. Chim. Acta*, 2005, **537**, 179.
49 Y. Yang, H. Yang, M. Yang, Y. Liu, G. Shen and R. Yu, *Anal. Chim. Acta*, 2004, **525**, 213.
50 H. Tang, F. Yen, Q. Tai and H. L. W. Chan, *Biosens. Bioelectron.*, 2010, **25**, 1646.

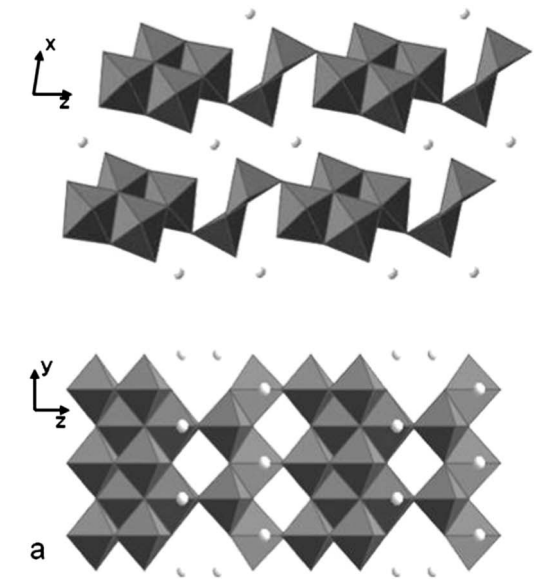

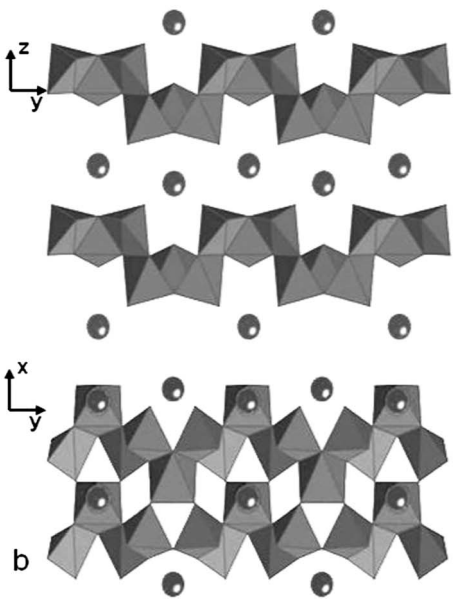

Fig. 1 (a) Projection of the structure of $Na[V_3O_8]\cdot 1.5H_2O$ along [010] and [100]. (b) Projection of the structure of $Cs[V_3O_8]$ along [100] and [001]. Interlayer cations are represented by white (Na^+) and grey (Cs^+) circles.

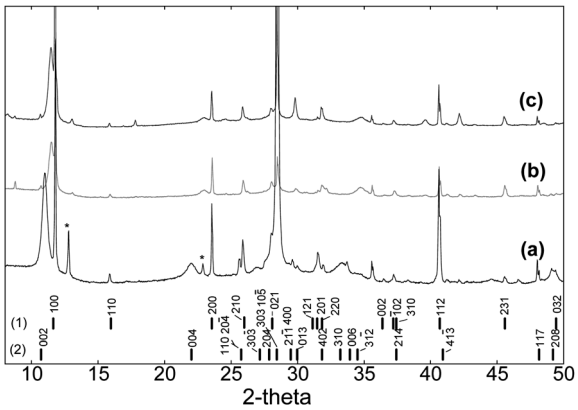

Fig. 2 Powder XRD patterns of (a) $K_2[V_6O_{16}]\cdot nH_2O$ at pH 3, (b) $K_2[V_6O_{16}]$–GOx biomembrane prepared by adsorption at pH 6 and (c) $K_2[V_6O_{16}]$–GOx biomembrane prepared by co-sedimentation ($K_2[V_6O_{16}]$–GOx_{cos}) at pH 6. (1) and (2) are respectively XRD patterns of $K_2[V_6O_{16}]\cdot 2.7H_2O$ and $K_2[V_6O_{16}]\cdot 1.5H_2O$ provided by the JCPDS card no. 51-379 and 54-0602. * corresponds to an impurity.

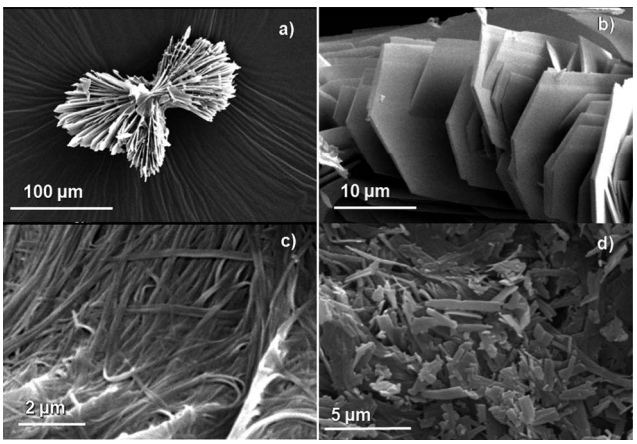

Fig. 3 SEM images of (a) and (b) $(NH_4)_2[V_6O_{16}]\cdot H_2O$ ($pH_i = 2$; ageing time = 4 days), (c) $(NH_4)_2[V_6O_{16}]\cdot 1.5H_2O$ ($pH_i = 3$; ageing time = 14 days) and (d) $K_2[V_6O_{16}]\cdot nH_2O$ ($n = 1.5$ and 2.7) at pH 3.

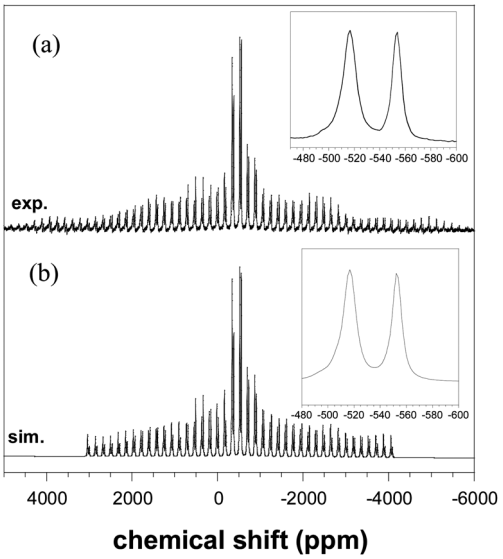

Fig. 4 (a) ^{51}V MAS NMR spectrum of $(NH_4)_2[V_6O_{16}]\cdot H_2O$ spun at 14 kHz and recorded at 79.0 MHz with 14 000 transients and (b) simulation obtained with QUASAR.

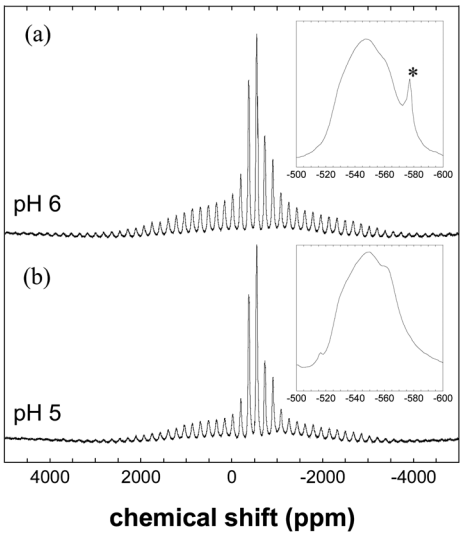

Fig. 5 ^{51}V MAS NMR spectrum of $K_2[V_6O_{16}]\cdot nH_2O$ spun at 14 kHz and recorded at 79.0 MHz with 14 000 transients. The spectra were recorded after immersing $K_2[V_6O_{16}]\cdot nH_2O$ precipitates in a solution of (a) phosphate buffer of pH 6 or (b) acetate buffer of pH 5 (* corresponds to an impurity).

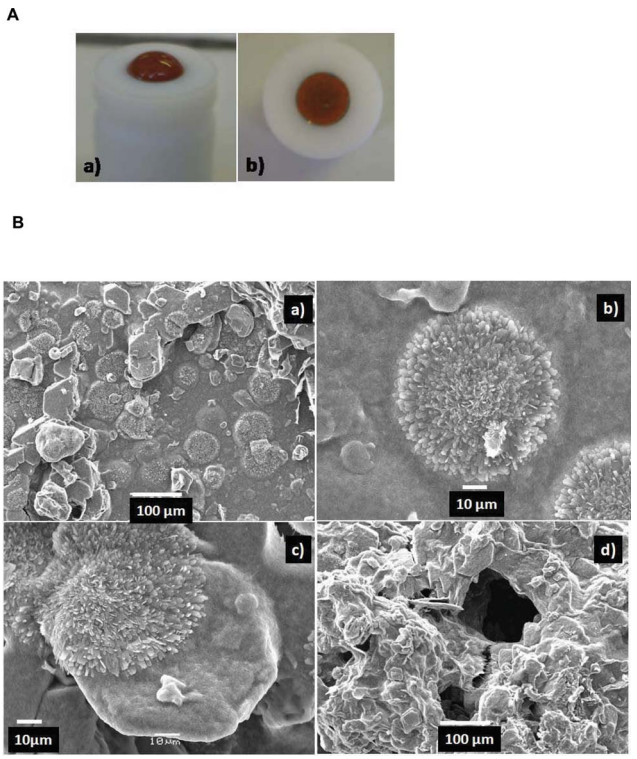

Fig. 6 (A) Photographs of (a) the suspension of $K_2[V_6O_{16}]$ deposited on a Pt electrode and (b) the dried $K_2[V_6O_{16}]$–GOx coating prepared by adsorption on the Pt electrode. (B) SEM images of (a), (b) and (c) $K_2[V_6O_{16}]$–GOx biomembrane prepared by adsorption, and (d) $K_2[V_6O_{16}]$–GOx biomembrane prepared by co-sedimentation.

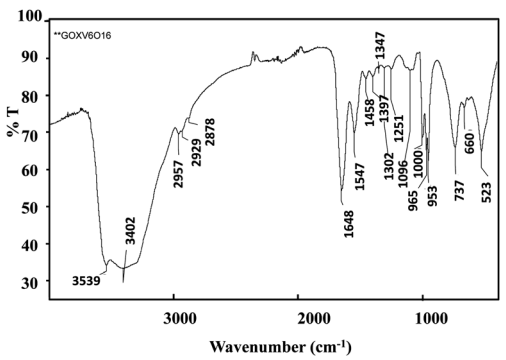

Fig. 7 Representative FT-IR spectrum of the $K_2[V_6O_{16}]$–GOx_{cos} biomembrane prepared by co-sedimentation.

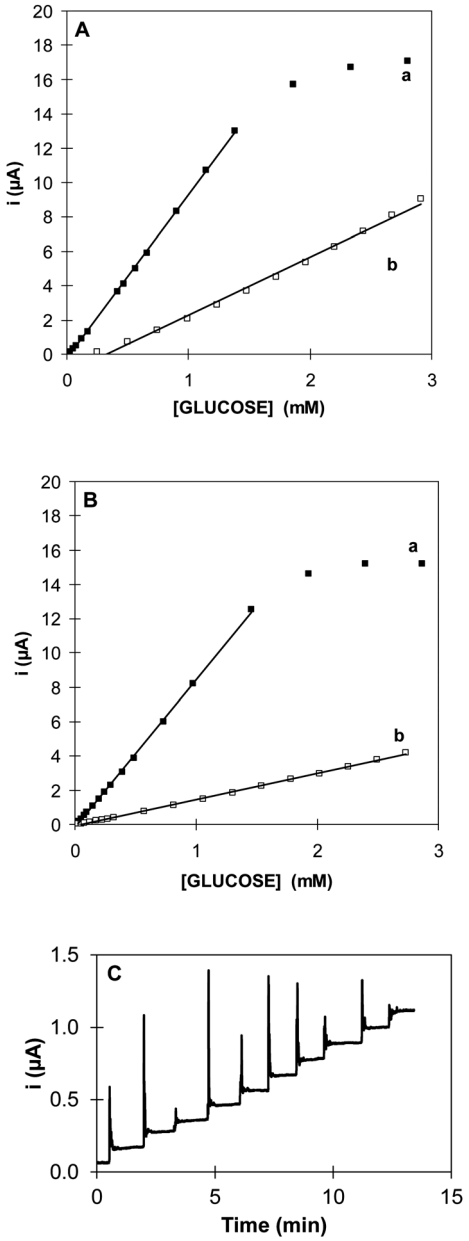

Fig. 8 Glucose calibration curves of (A) $K_2[V_6O_{16}]$–GOx (Ads, pH 6, curve a) and V_2O_5–GOx (Ads, pH 5, curve b); (B) $K_2[V_6O_{16}]$–GOx (Cos, pH 6, curve a) and V_2O_5–GOx (Cos, pH 5, curve b) (50 μg GOx, E_{app} = 0.7 V/Ag/AgCl). (C) Dynamic response after ten subsequent additions of 10 μM of glucose in phosphate buffer, pH 6 for the $K_2[V_6O_{16}]$–GOx_{cos} biosensor (50 μg GOx, E_{app} = 0.7 V/Ag/AgCl, Ads = adsorption, Cos = cosedimentation).

Electronic Supplementary Information (ESI) for Journal of Materials Chemistry

A general route to nanostructured $M[V_3O_8]$ and $M_x[V_6O_{16}]$ (x = 1 and 2) and their first evaluation for building enzymatic third generation biosensors.†

Nathalie Steunou,[*a,b] Christine Mousty,[c] Olivier Durupthy,[a] Cécile Roux,[a] Guillaume Laurent,[a] Corine Simonnet-Jégat,[b] Jacky Vigneron,[b] Arnaud Etcheberry,[b] Christian Bonhomme,[a] Jacques Livage,[a] and Thibaud Coradin.[a]

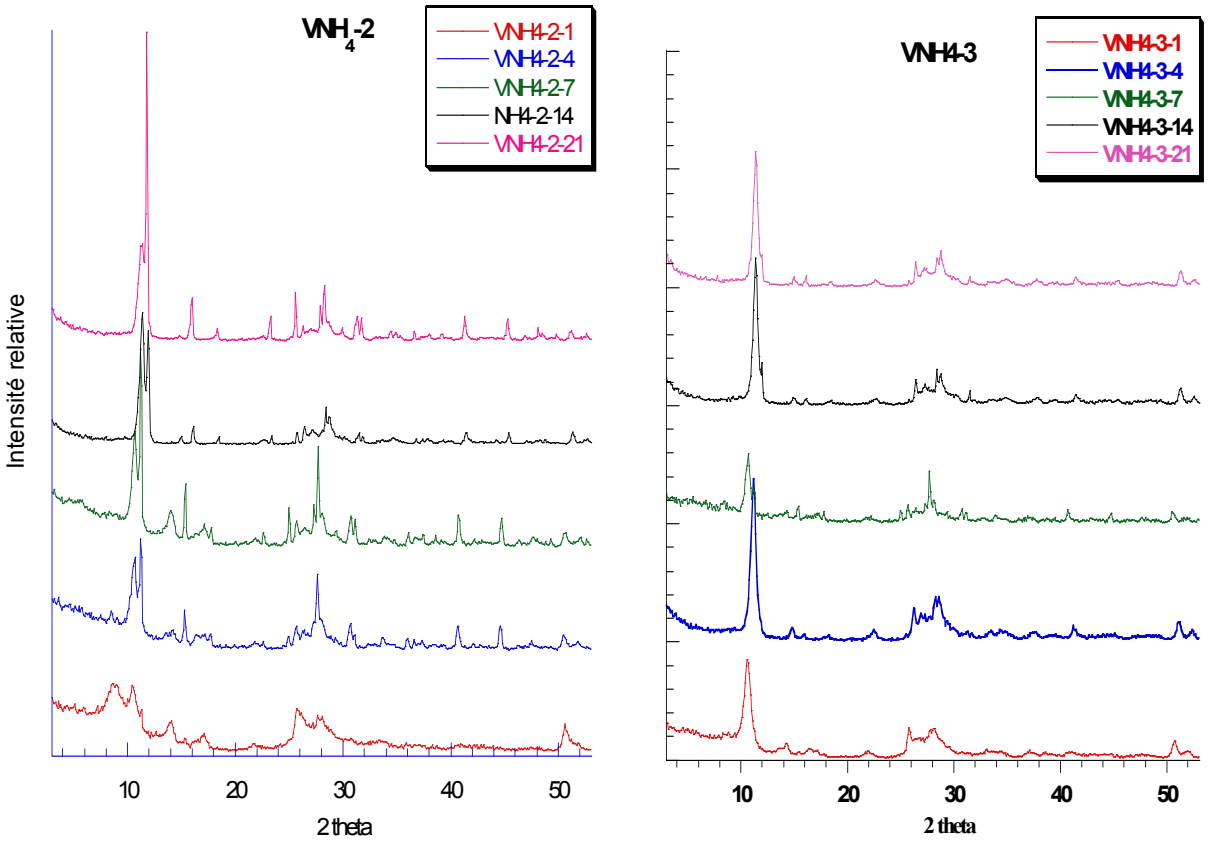

Fig. S1: X-ray diffraction patterns of $M[V_3O_8]$ and $M[V_6O_{16}]$ phases. In the title of figures VM-X-Y, M corresponds to the cation, X to the pH value and Y to the ageing time.

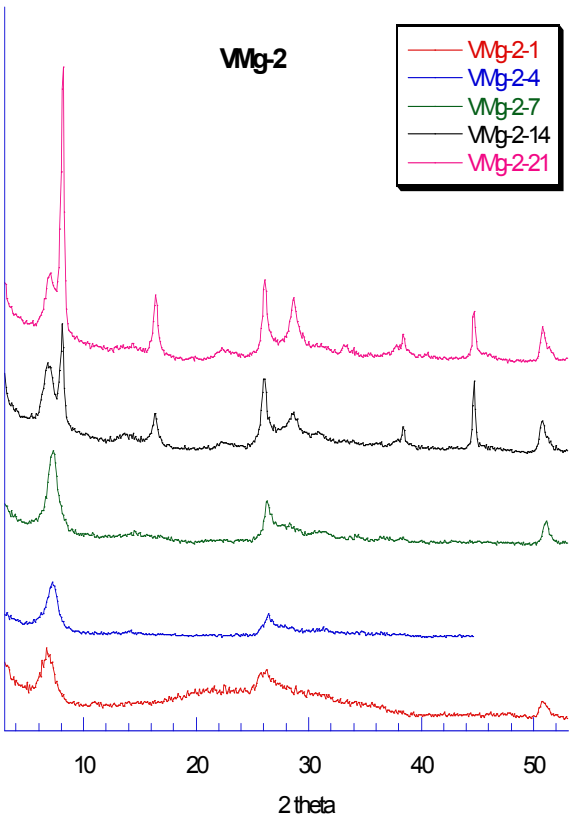

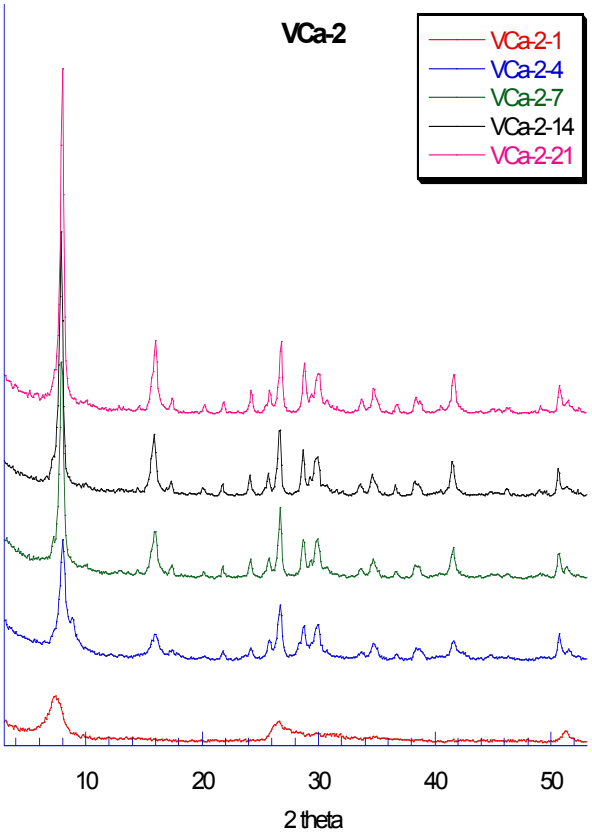

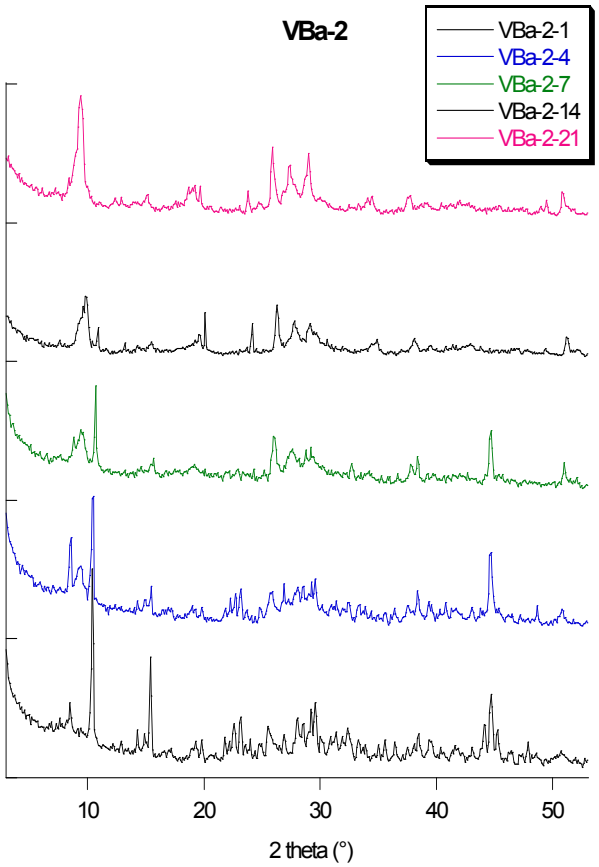

Fig. S1: X-ray diffraction patterns of M[V_3O_8] and M[V_6O_{16}] phases. In the title of figures VM-X-Y, M corresponds to the cation, X to the pH value and Y to the ageing time.

(a) A1

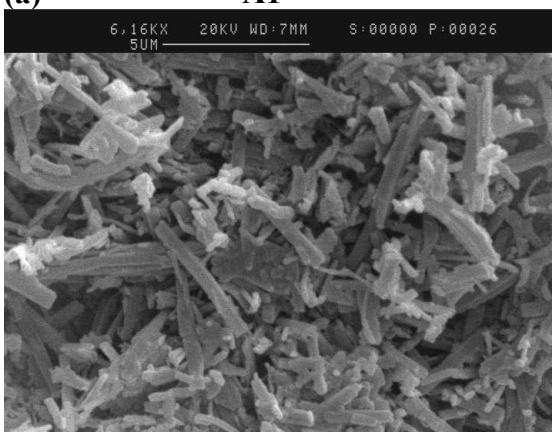

A2

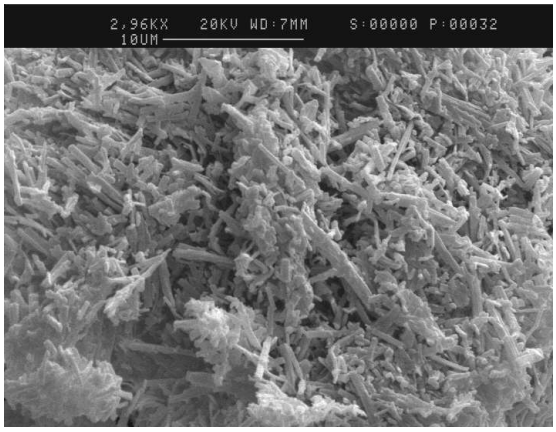

(b) B1

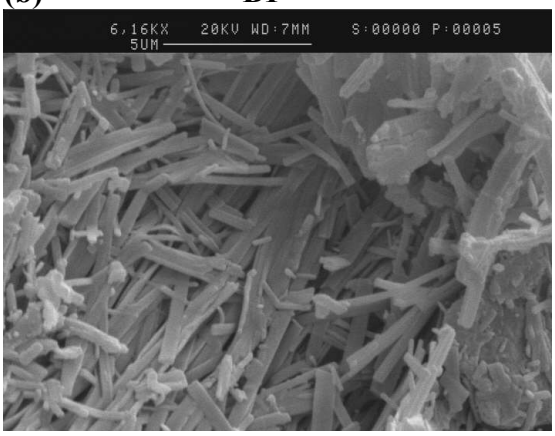

B2

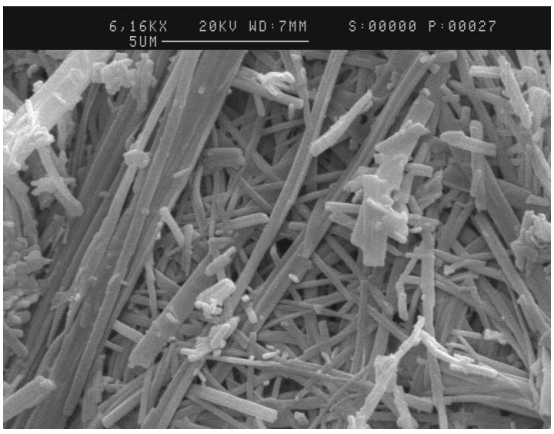

(c) C1

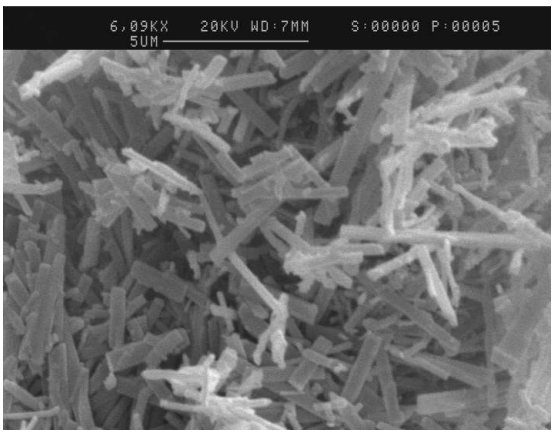

C2

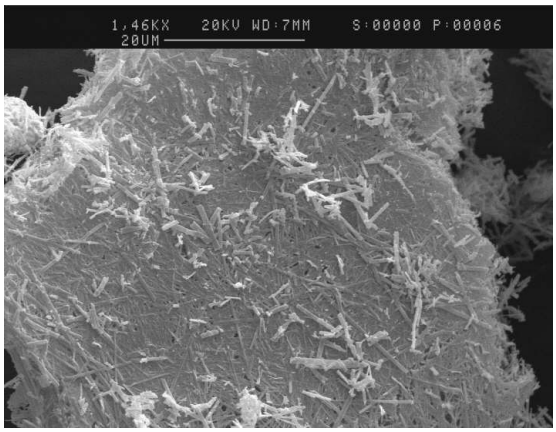

Fig. S2: SEM images for (a) $Mg[V_6O_{16}]7.1H_2O$ (images A1 and A2, pH_i = 2, 4 days); (b) $Ca[V_6O_{16}]\ 9.7H_2O$ (image B1 pH_i=2, 7 days) (image B2 pH_i = 3, 14 days) ; (c) $Ba_{1.2}[V_6O_{16}]5.5H_2O$ (images C1 and C2, pH_i =2, 14 days)

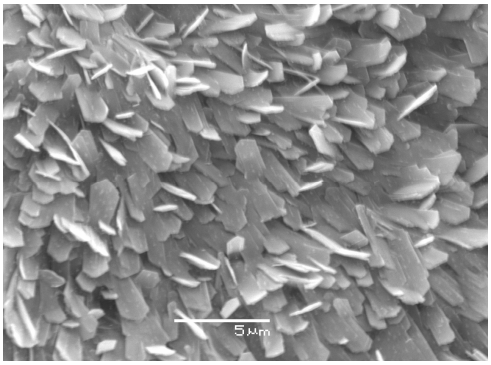

Fig S3. SEM images of $K_2[V_6O_{16}]$ -GOx biomembrane prepared by adsorption.

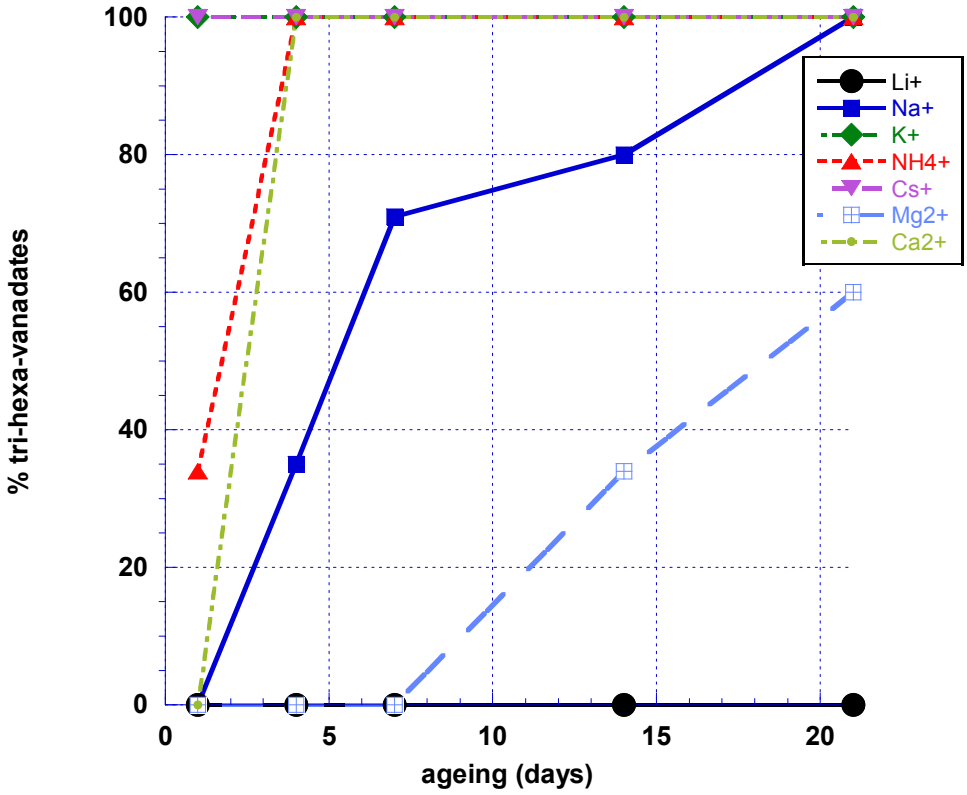

Fig S4: Relative amount of tri- and hexavanadates (i. e. m $(MV_3O_8/(m(MV_3O_8)+ m(V_2O_5))$ versus ageing at pH 2 for different monovalent and bivalent cations. The relative amount of $Ba_{1.2}[V_6O_{16}]$ is not reported because of the concomitant presence of $3Ba[V_{10}O_{28}]21H_2O$ in a significant amount.

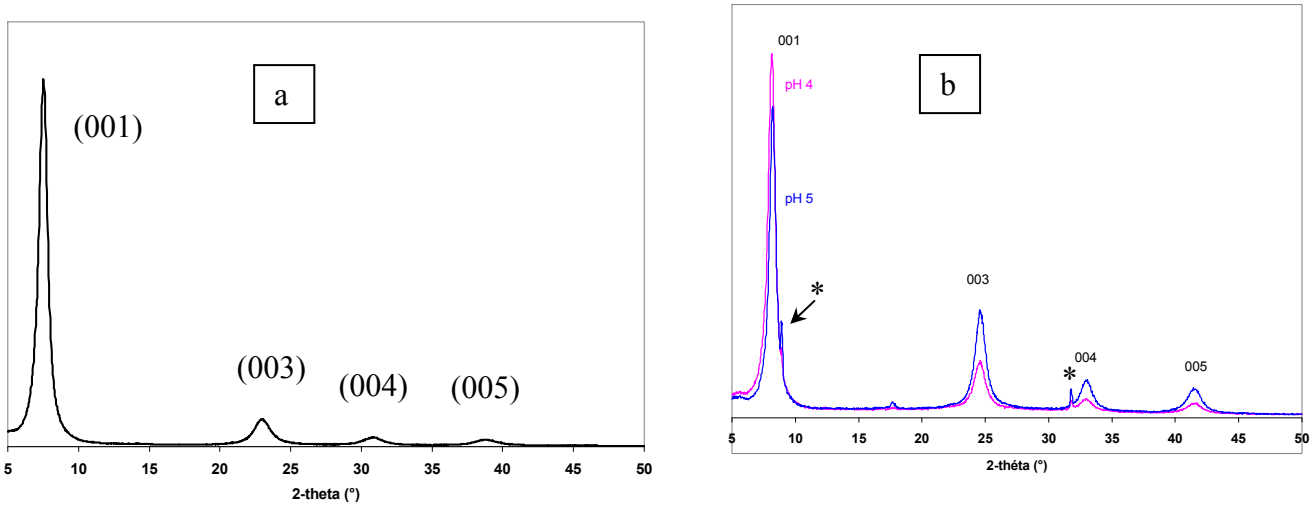

Fig. S5. XRD pattern of (a) $V_2O_5.nH_2O$ gel at pH 1, (b) $V_2O_5.nH_2O$ gel at pH 4 and 5.

For these experiments, $V_2O_5.nH_2O$ gels are deposited on glass substrates and the resulting films are immersed in acetate buffers of pH between 3 and 5. Due to the preferential orientation of V_2O_5 ribbon particles on flat surfaces, the XRD pattern of $V_2O_5.nH_2O$ gels at pH between 1 and 5 display only the series of 00ℓ reflections. The XRD diagrams of $V_2O_5.nH_2O$ gels at 3<pH<5 indicate that the structure of the gels is preserved until pH 5 despite of a little difference in the d_{001} value indicating a slight modification of the interlamellar space and the presence of an impurity of small amount at pH 5 (*).

The XRD pattern of V_2O_5 sol at pH 5 and $V_2O_5.nH_2O$-GOx biomembranes do not display XRD reflections. Actually, by redispersion of the gel in aqueous solution, the resulting V_2O_5 sol is then deposited on the glass substrate and dried. The stacking of V_2O_5 particles is not anymore present in the dried V_2O_5 film and the particles are completely disorganized. Since V_2O_5-GOx biomembrane results from the adsorption of enzyme onto these V_2O_5 films, no XRD reflections are present in the pattern of the $V_2O_5.nH_2O$-GOx biomembranes.

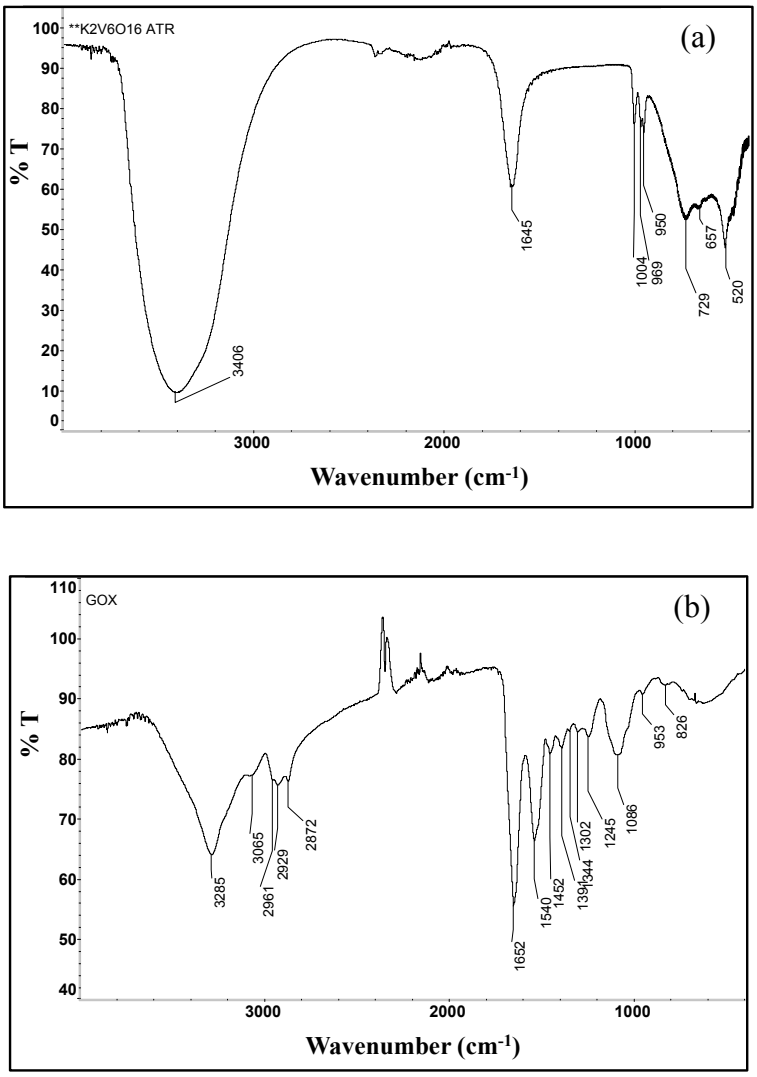

Fig. S6. Representative FT-IR spectra of pure a) $K_2[V_6O_{16}].nH_2O$ and b) GOx samples.

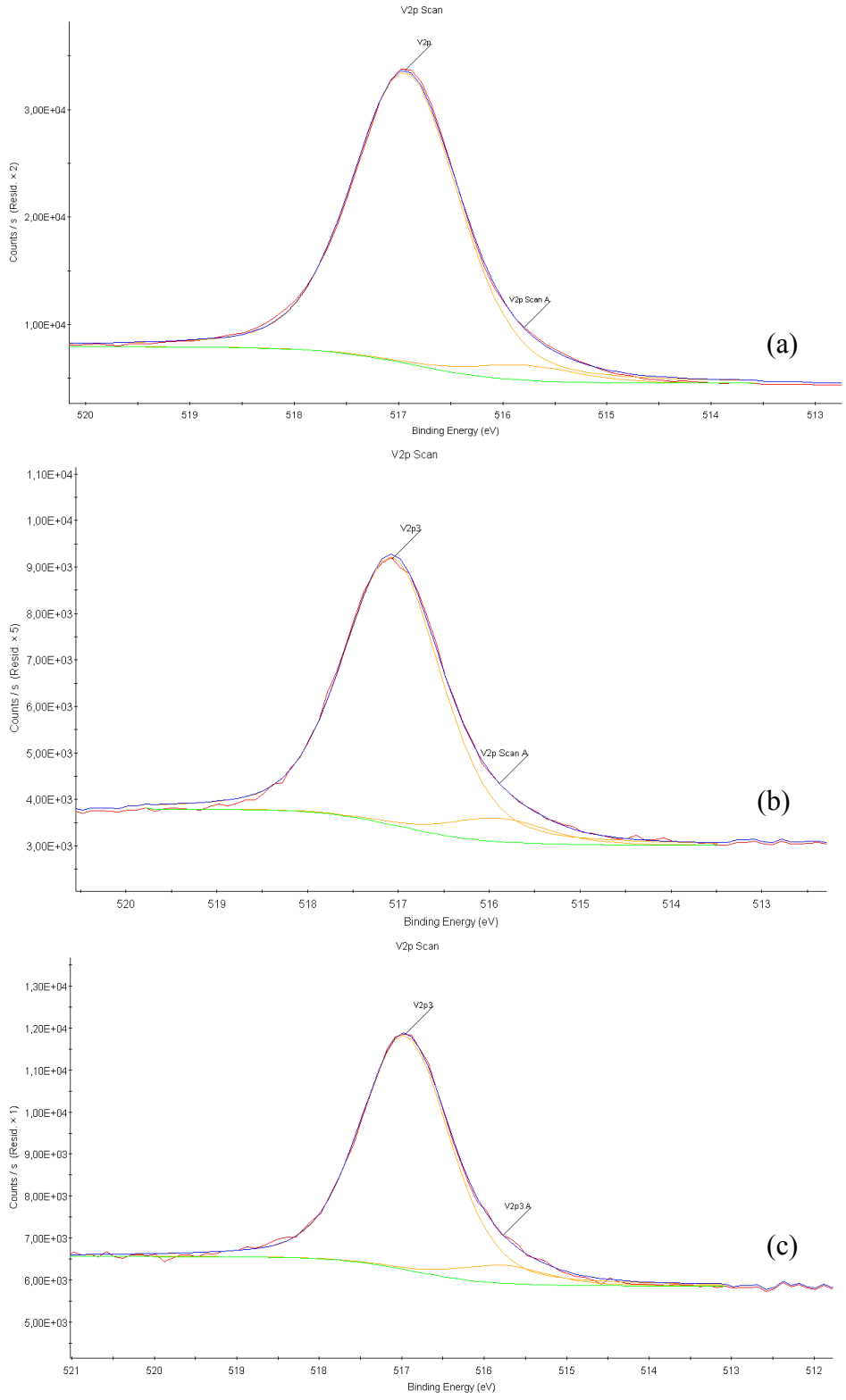

Fig. S7. V2p3/2 XPS spectra of a) $K_2[V_6O_{16}]$- pH 3, b) $K_2[V_6O_{16}]$- pH 6) c) $K_2[V_6O_{16}]$-GOx_{cos}

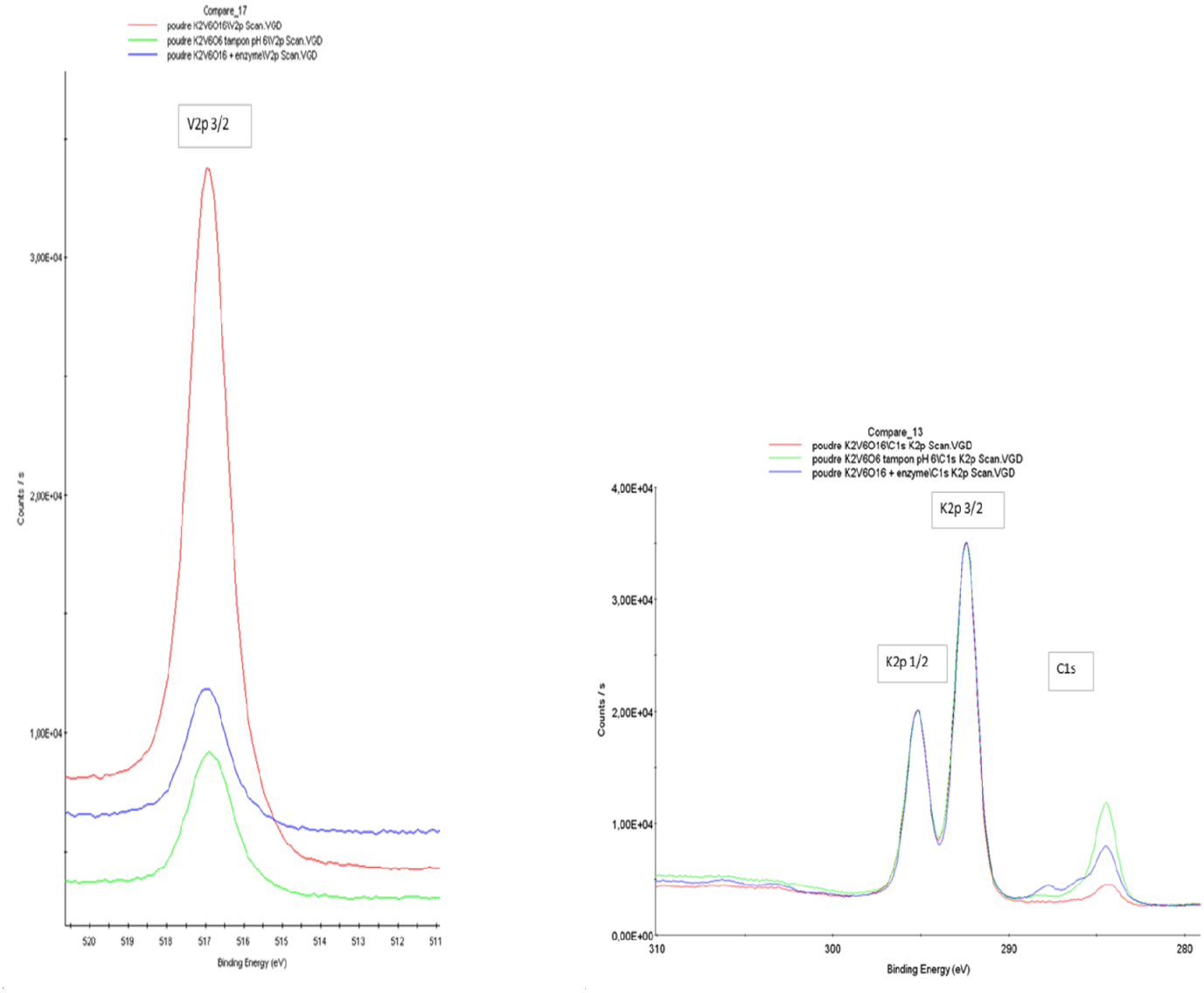

Fig. S8. Comparison of a) the V2p , b) K2p and C1s XPS spectra for $K_2[V_6O_{16}]$-pH 3, $K_2[V_6O_{16}]$-pH 6) and $K_2[V_6O_{16}]$-GOx_{cos}

Table S1. V2p 3/2 peak positions and atomic ratio for $K_2[V_6O_{16}]$-pH 3, $K_2[V_6O_{16}]$-pH 6) and $K_2[V_6O_{16}]$-GOx_{cos}

sample	Positions (eV)	Assignment	FWHM (eV)	Area (P) CPS.eV	%	$[V^{5+}]/[V^{4+}]$
$K_2[V_6O_{16}]$-pH 3	515.79 516.93	V2p Scan A (V^{4+}) V2p (V^{5+})	1.21 1.21	2028.43 39416.73	0.27 5.24	19.4
$K_2[V_6O_{16}]$-pH 6	515.89 517.07	V2p Scan A (V^{4+}) V2p3 (V^{5+})	1.28 1.28	767.73 8769.83	0.13 2.17	16.7
$K_2[V_6O_{16}]$-GOx_{cos}	515.77 516.96	V2p 3A (V^{4+}) V2p3 (V^{5+})	1.27 1.27	653.64 8519.45	0.11 1.38	12.5

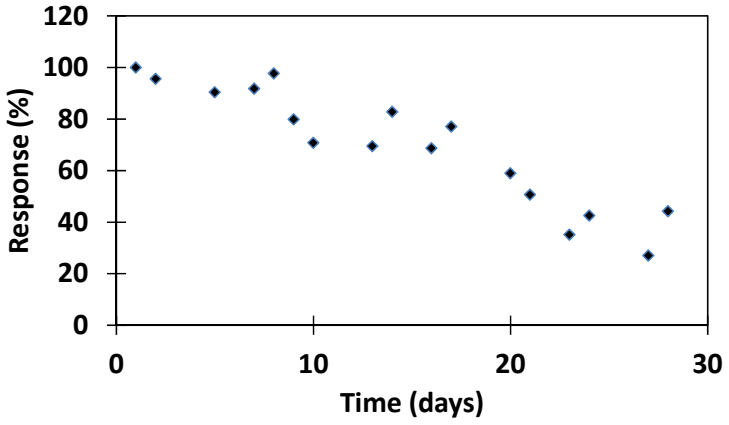

Fig. S9. Storage stability of the $K_2[V_6O_{16}]$-GOx_{cos} biosensor (pH 6.0)